Brain Structure and Function
https://doi.org/10.1007/s00429-022-02604-9

ORIGINAL ARTICLE

A spiking computational model for striatal cholinergic interneurons

Marcello G. Codianni[1] · **Jonathan E. Rubin**[1,2]

Received: 28 March 2022 / Accepted: 14 December 2022

Abstract
Cholinergic interneurons in the striatum, also known as tonically active interneurons or TANs, are thought to have a strong effect on corticostriatal plasticity and on striatal activity and outputs, which in turn play a critical role in modulating downstream basal ganglia activity and movement. Striatal TANs can exhibit a variety of firing patterns and responses to synaptic inputs; furthermore, they have been found to display various surges and pauses in activity associated with sensory cues and reward delivery in learning as well as with motor tic production. To help explain the factors that contribute to TAN activity patterns and to provide a resource for future studies, we present a novel conductance-based computational model of a striatal TAN. We show that this model produces the various characteristic firing patterns observed in recordings of TANs. With a single baseline tuning associated with tonic firing, the model also captures a wide range of TAN behaviors found in previous experiments involving a variety of manipulations. In addition to demonstrating these results, we explain how various ionic currents in the model contribute to them. Finally, we use this model to explore the contributions of the acetylcholine released by TANs to the production of surges and pauses in TAN activity in response to strong excitatory inputs. These results provide predictions for future experimental testing that may help with efforts to advance our understanding of the role of TANs in reinforcement learning and in motor disorders such as Tourette's syndrome.

Keywords Acetylcholine · Tonically active neurons · Conductance-based models · Bursting · Motor tics

Introduction

Despite comprising only about 2% of striatal neurons, tonically active cholinergic interneurons (TANs) are thought to play a crucial role in mediating striatal activity (Morris et al. 2004; Pakhotin and Bracci 2007; Witten et al. 2010; Kreitzer and Berke 2011; Brimblecombe et al. 2018; Zucca et al. 2018). These TANs are the primary identified striatal source of acetylcholine (ACh), and nearly all striatal neurons are thought to possess ACh-sensitive muscarinic receptors of various subtypes, particularly M1 and M2/4 (Giocomo and Hasselmo 2007; Kreitzer 2009). These receptors serve a number of roles, with M2 and M4 acting to inhibit firing and M1 yielding more complex effects that allow for the promotion of firing (Howe and Surmeier 1995; Ding et al. 2006; Ishii and Kurachi 2006). Recently, there has been a focused interest in the ways that ACh may impact or contribute to corticostriatal plasticity (Centonze et al. 2003; Morris et al. 2004; Brimblecombe et al. 2018; Zucca et al. 2018; Nosaka and Wickens 2022), to various basal ganglia-related neurological disorders, such as Parkinson's disease and Tourette's syndrome (Calabresi et al. 2000; Pisani et al. 2007; Ding et al. 2006; McKinley et al. 2019; Moehle and Conn 2019), and to the role of TANs in levodopa-related dyskinesia (Perez-Lloret and Barrantes 2016; Lim et al. 2015; Ding et al. 2011). Although TANs are prominent at the forefront of striatal research, there are few mathematical models of these neurons. Developing such models represents an important step in advancing this research, to provide a tool for hypothesis testing and generating mechanistic predictions.

Experimental recordings have provided observations of TAN activity patterns, as well as insights into the nature and properties of the individual currents expressed in TANs (Wilson 2005; Choi et al. 2020). Given the availability of this level of information about TANs, we sought to develop

✉ Jonathan E. Rubin
jonrubin@pitt.edu

Marcello G. Codianni
mac384@pitt.edu

[1] Department of Mathematics, University of Pittsburgh, Pittsburgh, PA 15260, USA

[2] Center for the Neural Basis of Cognition, Pittsburgh, PA 15260, USA

Published online: 18 January 2023

a conductance-based model that includes experimentally observed currents and to find parameter regimes in which various TAN behaviors are captured. Further, there are numerous reports characterizing TAN activity under various experimental conditions (Bennett et al. 2000; Goldberg and Wilson 2005; Wilson 2005; Wilson and Goldberg 2006; Aosaki et al. 2010; Zucca et al. 2018; Zhang et al. 2018; Choi et al. 2020), and we tuned parameters to identify a regime in which our model matches these experimental benchmarks at a qualitative and, when possible, quantitative level.

Finally, we used the model to simulate the dynamics of TANs, along with spiny projection neurons (SPNs), in response to a strong excitatory synaptic input. Such signals, associated with reward-related sensory stimuli, lead to patterns of surges and pauses in TAN spiking, and similar surge–pause patterns are observed both in TANs and in SPNs in association with tic production in an animal model of Tourette's syndrome (TS). Specifically, in an extension of our new TAN model, we considered the ACh dynamics resulting from a surge in TAN firing and the resulting effects of ACh on TANs and SPNs. We consider two mechanisms that could underlie these effects: cholinergic effects directly on the effective input associated with surge initiation and autoregulation effects of heightened ACh on the TANs themselves. We show that with the combination of these two components, the model can reproduce the TAN surge–pause pattern and in particular the TAN and SPN dynamics observed experimentally in animal models where the striatal application of bicuculline yields motor tic production (Bronfeld et al. 2011, 2013). Thus, we predict that both of these impacts of ACh release contribute to the surge and pause response and its functional implications.

Materials and methods

Overview of model components

We develop a single-compartment, conductance-based model of a striatal TAN, which we simulate using XPPAUT (Ermentrout 2002). In addition to typical sodium, potassium, and leak currents (I_{Na}, I_K, and I_L, respectively), the core model includes a variety of other currents identified in TANs: sag and inward rectifier currents (I_h and I_{IR}), depolarization-activated (I_{Ca}) and T-type (I_T) calcium currents, medium and slow afterhyperpolarization (AHP) currents (I_{mAHP} and I_{sAHP}), a persistent sodium current (I_{NaP}), and an M-type potassium current I_M (sometimes called persistent K) (Nisenbaum et al. 1996; Song et al. 1998; Gabel and Nisenbaum 1999; Bennett et al. 2000; Maurice et al. 2004; Zhou et al. 2002; Wilson 2005; Wilson and Goldberg 2006; Pisani et al. 2007; Tan and Bullock 2008; Goldberg et al. 2009; Goldberg and Reynolds 2011; Krishnan et al. 2016; Zhang et al. 2018; Abudukeyoumu et al. 2019; Gritton et al. 2019; McKinley et al. 2019; Choi et al. 2020). In addition to the gating variables associated with these currents, the core model includes dynamics of the concentrations of intracellular calcium ($[Ca]$), which affects the conductance of an AHP current, extracellular potassium (K_o), and intracellular sodium (Na_i) ions (Barreto and Cressman 2011). Finally, our model allows for inputs, which can be experimentally applied or synaptic, and includes an additive noise term, which we activate in some specific simulations.

In the later parts of the paper, we present simulations for which the model is augmented to include some more phenomenological components. Specifically, the augmented model incorporates dynamics of the local levels of ACh, which is released by TAN spiking, along with the feedback effects of ACh on other model components, including glutamatergic inputs. There appear to have been few quantitative measurements related to its dynamics and its effects as mediated through muscarinic receptors (M1, M2, and M4), although the latter have been characterized qualitatively (Zhang et al. 2002; Kim et al. 2019). Thus, we implement its dynamics as follows: ACh is released into the extracellular space by TANs at a rate that depends on TAN spiking, while after its release, ACh binds and unbinds to different receptors at associated rates and is also degraded at some rate by acetylcholinesterase (AChE) (Fig. 1). We also consider dynamics of a model striatal spiny projection neuron (SPN) (McCarthy et al. 2011) when we simulate the augmented model, since SPNs have been recorded along with TANs during motor tic production (Bronfeld et al. 2011, 2013). We do not include synaptic inhibition from the model SPN to the model TAN, because the relevant experimental model includes the application of bicuculline (Bronfeld et al. 2011,

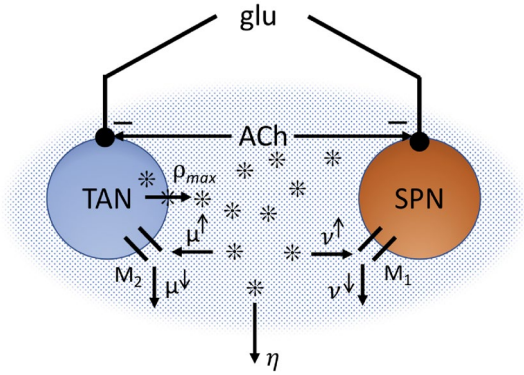

Fig. 1 Diagram of cell interactions. Acetylcholine (ACh) is released at a baseline rate ρ_{max} from spiking TANs and is degraded by AChE at a rate η. Extracellular ACh becomes bound and unbound to M_2 and M_1 receptors on TANs and SPNs at rates $\mu^{\uparrow,\downarrow}$ and $\nu^{\uparrow,\downarrow}$, respectively. ACh also binds to receptors that modulate glutamatergic inputs (glu) to these neurons

2013), which we assume, for simplicity, induces a complete block of inhibition.

Others (Stiefel et al. 2008; Fink et al. 2011; McCarthy et al. 2011; Fink et al. 2013; Krishnan et al. 2016) have modeled the effects of different fixed levels of neuromodulators in conductance-based models by adjusting maximal conductance levels in the currents impacted by these factors. Moving beyond this quasi-static viewpoint, we model the temporally evolving effects of ACh on receptor activation through the dynamics of various conductances. Of particular interest, we include a spike-enhancing M1 current in the SPN model (Shen et al. 2005; Kondabolu et al. 2016), a spike-reducing M2/4 current in the TAN model, and M2/4-like suppression of glutamatergic inputs to both model cells (Kreitzer 2009; Dolezal and Wecker 1990).

Core TAN model details

The current balance equation for our model TAN takes the form

$$\begin{aligned} C_T \tfrac{d}{dt} v_T = &- I_{Na} - I_K - I_L - I_h - I_{IR} \\ &- I_{Ca} - I_{sAHP} - I_{mAHP} \\ &- I_T - I_{NaP} - I_{MT} \\ &+ I_{app} + \zeta_T W_T(t), \end{aligned} \tag{1}$$

where the subscript T (other than in the T-type calcium current) stands for TAN. The currents are given in the Hodgkin–Huxley formulation as

$$\begin{aligned} I_{Na} &= g_{Na} m_\infty^3(v) h (v - E_{Na}) \\ I_K &= g_K n^4 (v - E_K) \\ I_L &= g_L (v - E_L) \\ I_h &= g_h p (v - E_h) \\ I_{IR} &= g_{IR} \left(1 / \exp\left(\tfrac{v - \theta_{IR}}{\sigma_{IR}} \right) \right) (v - E_K) \\ I_{Ca} &= g_{Ca} s^2 (v - E_{Ca}) \\ I_{sAHP} &= g_{sAHP} \xi (v - E_K) \\ I_{mAHP} &= g_{mAHP} ([Ca]/([Ca] + k_m))(v - E_K) \\ I_T &= g_T a^3 (v - E_{Ca}) \\ I_{NaP} &= g_{NaP} r (v - E_{Na}) \\ I_{MT} &= g_{M2/4} m_T (v_T - E_K). \end{aligned} \tag{2}$$

The term I_{app} in Eq. (1) denotes a parameter that we make non-zero in some specific simulations to simulate manipulations performed in past experiments. The term $W_T(t)$ refers to a Wiener process used to include noise in certain simulations, with a scalable amplitude ζ_T. In most cases, we found that the inclusion of noise did not significantly alter the qualitative behavior of the model TAN, and so, it is excluded from TAN simulations (i.e., $\zeta_T = 0$) unless otherwise noted.

Functions and dynamics related to the sodium and potassium activation variables m, n and the sodium inactivation variable h are adapted from Corbit et al. (2016). The fast activation for I_{Na} is treated as instantaneous, $m = m_\infty(v)$, where $m_\infty(v)$ takes the form

$$m_\infty(v) = -0.1(v + 28)/\tau_m(v)$$

for

$$\begin{aligned} \tau_m(v) = &-0.1(v + 28) + 4\{\exp[-0.1(v + 28)] - 1\} \\ &\exp[-(v + 53)/18] \end{aligned}$$

The other gating variables in the TAN model obey differential equations that are a standard part of the Hodgkin–Huxley framework, of the form

$$\frac{d}{dt} X = (X_\infty(v) - X)/\tau_X. \tag{3}$$

For h and n, the function $X_\infty(v)$ is determined by $\alpha_X(v) = X_\infty(v)/\tau_X$ and $\beta_X(v) = (1 - X_\infty(v))/\tau_X$ where

$$\begin{aligned} \alpha_h(v) &= 0.35 \exp((-v + 51)/20), \\ \beta_h(v) &= 5/(\exp(-(v + 21)/10) + 1), \\ \alpha_n(v) &= -.05(v + 27/(\exp[-(v + 27)/10] - 1)), \\ \beta_n(v) &= -0.625 \exp(-(v + 37)/80). \end{aligned}$$

Otherwise, activation and inactivation variables evolve under Eq. (3) with $X_\infty(v) = 1/\left(1 + \exp\left(\frac{v - \theta_X}{\sigma_X}\right)\right)$ for parameters τ_X, θ_X, and σ_X specific to each variable. The starting values used for these parameters were taken from past models of the respective currents (Wilson 2005; McCarthy et al. 2008; Terman et al. 2002); from there, parameters were adjusted manually to obtain agreement with experimental benchmarks. The baseline values used are presented in Table 1; here, τ_x, θ_X, and σ_X denote the time constant, half activation (inactivation), and slope of the function X_∞, respectively, for each X. As we present our results, the importance of certain relations among parameters as well as the effects of varying some key parameters will be discussed.

Additional model components include the calcium-related equations

$$\begin{aligned} \tfrac{d}{dt}[Ca] &= \epsilon(-I_{Ca}(v) - k_{Ca}[Ca] - I_T(v)), \\ \tfrac{d}{dt}\xi &= a_\xi [Ca](1 - \xi) - b_\xi \xi \end{aligned}$$

and ion concentration equations

$$\begin{aligned} \tau_{K_o} \tfrac{d}{dt} K_o &= \gamma I_K - 2 I_{pump} - I_{glia} - I_{diff}, \\ \tau_{Na_i} \tfrac{d}{dt} Na_i &= -\gamma I_{Na} - 3 I_{pump} \end{aligned}$$

Table 1 Main TAN model parameters

Parameter	Value
C_T (μF/cm^2)	1
g_{Na} (mS/cm^2)	25
g_K (mS/cm^2)	15, 10†
g_{IR} (mS/cm^2)	2.75
g_h (mS/cm^2)	1.5, 0.8††
g_T (mS/cm^2)	0.15
g_{Ca} (mS/cm^2)	0.1
g_{NaP} (mS/cm^2)	0.1
g_{sAHP} (mS/cm^2)	10
g_{mAHP} (mS/cm^2)	15, 60†
$g_{exc-max_T}$ (mS/cm^2)	0.065
$g_{exc-max_S}$ (mS/cm^2)	0.065
Δ	0.01
g_L (mS/cm^2)	0.08
E_h (mV)	− 60
E_{NaP} (mV)	45
E_L (mV)	− 53
θ_{IR} (mV)	− 87
σ_{IR} (mV)	5.5
θ_p (mV)	− 90
σ_p (mV)	6
τ_p (ms)	600, 1200†
θ_a (mV)	− 63
σ_a (mV)	7.8
θ_s (mV)	140
σ_s (mV)	4
θ_r (mV)	− 50
σ_r (mV)	3.1
τ_r (ms)	1
k_{Ca}	22.5
τ_T, τ_S (ms)	100
a_ξ	0.5
b_ξ	0.05
k_m	15
ε	0.0001
ζ_T	0, 8*

†Denotes values used for experiments with apamin application, †† Denotes values used for burst firing, and *Denotes value used for noisy irregular firing

with

$$I_{pump} = \rho / \left(1 + \exp\left(\frac{25 - Na_i}{3}\right)\right) \times \left(1/\left(1 + \exp\left(5.5 - K_o\right)\right)\right),$$

$$I_{glia} = 20 / \left(1 + \exp\left(\frac{18 - K_o}{2.5}\right)\right),$$

$$I_{diff} = \varepsilon_{diff}(K_o - K_{base}).$$

Table 2 Ion subsystem parameters

Parameter	Value
γ	0.04
δ	1
ρ	1.25
ε_{diff}	1.333
K_{base}	4.2, 3.7**
τ_{K_o}	1000
τ_{Na_i}	1000

**Denotes value used for burst firing

These concentrations affect the potassium and sodium reversal potentials, respectively, given by

$$E_K = 26.64 \log\left(\frac{K_o}{K_i}\right),$$

$$E_{Na} = 26.64 \log\left(\frac{Na_o}{Na_i}\right),$$

where $K_i = 118 - Na_i$ and $Na_o = 162 - Na_i$ (Barreto and Cressman 2011) (see Table 2 for parameter values).

Augmented model including ACh

ACh affects the conductances of various currents that contribute to TAN dynamics, so we develop an extension to the model that can be appended to the core model to explore activity for which ACh release and dynamics may be important, and otherwise can be ignored. Since there is a lack of experimental data carefully characterizing the quantitative properties of ACh dynamics, we developed a phenomenological representation of this dynamics as well as its impact on factors contributing to TAN and SPN behavior. We do not attempt to provide an explicit mapping between ACh model components and specific biological factors, such as astrocytic effects on ACh levels.

Table 3 Cholinergic subsystem parameters

Parameter	Value
η	0.005
ρ_{max}	10
θ_ρ	1
σ_ρ	− 0.1
α	2
$\mu^\uparrow$	0.01
$\mu^\downarrow$	0.01
$\nu^\uparrow$	0.01
$\nu^\downarrow$	0.03

Here, we introduce our phenomenological model for the dynamics of the level of free ACh, which we denote by A and which depends on TAN firing, along with variables A_T, A_S, A_{exc} representing various bound pools of ACh. We assume that this model represents ACh release by synchronized firing of many TANs, as would be induced by a strong, shared input. The model consists of the differential equations (see Table 3 for parameter values)

$$\begin{aligned}\frac{d}{dt}A &= \rho_{max}/\left(1+\exp\left(\frac{v_T-\theta_\rho}{\sigma_\rho}\right)\right) - \eta A \\ &\quad - \tau^*\left(\frac{A^2}{A^2+\alpha^2} - A_{exc}\right) - \mu^{\uparrow}A + \mu^{\downarrow}A_T \\ &\quad - \nu^{\uparrow}A + \nu^{\downarrow}A_S \\ \frac{d}{dt}A_T &= \mu^{\uparrow}A - \mu^{\downarrow}A_T \\ \frac{d}{dt}A_S &= \nu^{\uparrow}A - \nu^{\downarrow}A_S \\ \frac{d}{dt}A_{exc} &= \tau^*\left(\frac{A^2}{A^2+\alpha^2} - A_{exc}\right).\end{aligned} \tag{4}$$

In system (4), ρ_{max} and the sigmoid function that it multiplies represent the rate of voltage-dependent release of ACh by elevations in TAN voltage (spikes) and η represents the rate of degradation of ACh by AChE. The variables A_T, A_S denote levels of ACh bound to M-receptors on TANs and SPNs (discussed further below), respectively. The parameters $\mu^{\uparrow,\downarrow}$ and $\nu^{\uparrow,\downarrow}$ represent M-receptor binding and unbinding rates of ACh for TANs and SPNs, respectively, and τ^* is included for unit conversion and is set to 1 ms^{-1}. Indeed, note that these phenomenological equations are dimensionless and the variables involved should not be viewed as concentrations. Finally, A_{exc} represents the level of binding of ACh to receptors that modulate glutamatergic inputs to TANs and SPNs, which occurs with a half-saturation level α (i.e., when $ACh = \alpha$, A_{exc} equilibrates to 0.5); correspondingly, a term equal to $-dA_{exc}/dt$ is included in the equation for the rate of change of ACh. Although we do not know of experimental results that precisely quantify the kinetic parameters associated with these processes, we chose values to yield sensitivity of ACh levels to TAN spike patterns, as shown in recent findings (Nosaka and Wickens 2022).

TANs and SPNs are known to receive glutamatergic input from thalamus and cortex (Kreitzer 2009; Ding et al. 2010; Assous et al. 2017; Abudukeyoumu et al. 2019). Because these input sources target TANs and SPNs with different intensities, the overall glutamatergic input signals to these two populations are likely to differ. In this paper, however, we will simply test the impact of a few simple input patterns on TAN and SPN activity, and hence, we simply consider an overall glutamatergic current to each population. For simplicity's sake, we do not distinguish between cortical and thalamic inputs into each cell type, but rather combine all external currents to each neuron into a single applied current term. To account for the differences in their inputs, we consider inputs to the model TAN and SPN independently, given by the I_{appT} and I_{appS} terms in their respective model equations.

We use the TAN model to simulate TAN behavior in a variety of scenarios implemented in the previous experiments. In those experiments in which TTX is applied to the bath, there is no firing, and hence no ACh release (Figs. 2, 3, 6). As stated above, our ACh model components are meant to represent ACh dynamics associated with synchronized firing of many TAN cells. In those experiments in which only individual cells were being stimulated at any given time, only a comparatively small amount of ACh would be released. Rather than running our single-cell simulations with vastly down-scaled ACh levels that have no effect on the results, we sped them up by simply excluding ACh dynamics during our simulations of these effects (Figs. 7, 8). In the in vitro experiments involving apamin, apamin was applied to the bath; hence, we treat our model cell's activity as characteristic of the activity that would occur in many TAN neurons, and thus, we include ACh effects in these simulations (Fig. 9). Similarly, in experimental recordings of baseline firing modes, the entire TAN population is free to fire, so we maintain dynamic cholinergic effects in the model (Figs. 2, 3).

To simulate the TAN response to reward-related excitatory stimuli and the neural activity observed under striatal bicuculline application shown to yield motor tic production, we provided both the TAN and the SPN with an excitatory input spike train that was either ACh-sensitive, with dynamics given by Eqs. (6), (7), (4), or ACh-insensitive, with fixed input conductance $g_{exc-max_*}$. Experimentally, in motor tic episodes in the bicuculline animal model, the onset of SPN activity preceded the onset of TAN activity by about 50 ms (Bronfeld et al. 2011), so we supplied the SPN with an input that originated 50ms before the input to the TAN.

Now, we describe how ACh affects components of the TAN model. First, we note that for the M-current in the model, the gating variable m_T obeys Eq. (3); however, the maximal conductance $g_{M2/4}$ can be modulated by the effects of ACh on associated M-type receptors through a G-protein-dependent second messenger type system (Ishii and Kurachi 2006). Thus, in the augmented model, we set $g_{M2/4} = (g^{const}_{M2/4} + g^{dyn}_{M2/4})/2$, where $g^{const}_{M2/4}$ denotes a fixed, ACh-insensitive conductance term and $g^{dyn}_{M2/4}$ represents a dynamic, ACh-sensitive conductance term, with

$$\tau_{gT}\frac{d}{dt}g^{dyn}_{M2/4} = g_{M2/4max}/\left(1+\exp\left(\frac{A_T-\theta_{gT}}{\sigma_{gT}}\right)\right) - g^{dyn}_{M2/4}. \tag{5}$$

Rather than voltage, this conductance equation depends on A_T, which represents the level of ACh bound to M-type receptors on TANs, as described below.

Second, in the augmented model, we also include synaptic inputs with an ACh-dependent component. Specifically, on the right-hand side of Eq. (1), we subtract a

glutamatergic input current with maximal conductance $g_{exc_T} = (g^{const}_{exc_T} + g^{dyn}_{exc_T})/2$ with $g^{const}_{exc_T}$ fixed and $g^{dyn}_{exc_T}$ dynamic, governed by the equation

$$\tau_{exc_T}\frac{d}{dt}g^{dyn}_{exc_T} = g_{exc-max_T}/\left(1+\exp\left(\frac{A_{exc}-\theta_{app_T}}{\sigma_{app_T}}\right)\right) - g^{dyn}_{exc_T}. \tag{6}$$

To generate the synaptic input current, we start from a Poisson spike train with a firing rate determined by what we call a boxcar or a ramp. A boxcar spike train begins firing at a high rate (we use 80 Hz unless otherwise noted) at time t_0 and turns off at time $t_f = t_0 + \Delta_B$; we use 250ms as our default value for Δ_B. A ramp spike train begins firing at a high rate (again, 80 Hz) at time t_0 and the rate then decays linearly to reach 0 Hz at time $t_f = t_0 + \Delta_R$, with a default value $\Delta_R = 2000$ms. For ACh-sensitive currents, these values define an envelope for the effective input, which is modulated by A_{exc}. We denote the fraction of maximal excitation impacting each TAN by w_T; this quantity is augmented via $t = t_{spike} : w_T \mapsto w_T + \Delta$ at each spike time t_{spike} and decays exponentially via $\tau_{w_T}\frac{d}{dt}w_T = -w_T$ in between spikes. Since we choose 0 mV as the excitatory synaptic reversal potential, the total synaptic input current to an augmented model TAN with voltage v_T is given by $g_{exc_T} w_T v_T$.

The terms A_T and A_{exc} in Eqs. (5), (6) refer to levels of bound ACh, with A_T for TAN M-receptors and A_{exc} for receptors that modulate incoming synaptic currents. In some simulations, we also include SPNs, and ACh can bind to SPN M-receptors, as well. We use a spiking SPN model adapted from past work by McCarthy et al. (2008). The current balance equation for this model takes the form

$$C_S\frac{d}{dt}v_S = -\ I_{Na} - I_K - I_{leak} - I_{MS} - g_{excS}w_s v_s + \zeta_S W_S(t),$$

where

$$\begin{aligned}
I_{MS} &= g_{M1}m_S(v_S - E_K)\\
g_{M1} &= \frac{g^{const}_{M1} + g^{dyn}_{M1}}{2}\\
\tau_{gS}\frac{d}{dt}g^{dyn}_{M1} &= g_{M1max}/\left(1+\exp\left(\tfrac{A_S-\theta_{gS}}{\sigma_{gS}}\right)\right)\\
&\quad - g^{dyn}_{M1}\\
g_{exc_S} &= \frac{g^{const}_{exc_S} + g^{dyn}_{exc_S}}{2}\\
\tau_{app_S}\frac{d}{dt}g^{dyn}_{exc_S} &= g_{exc-max_S}/\left(1+\exp\left(\tfrac{A_{exc}-\theta_{app_S}}{\sigma_{app_S}}\right)\right) - g^{dyn}_{exc_S}\\
\frac{d}{dt}m_S &= (\alpha_{mS}(v_S)/[\alpha_{mS}(v_S)+\beta_{mS}(v_S)] - m_S)/\tau_{mS}(v_S)\\
\alpha_{mS}(v_S) &= (3.209\times10^{-3})(v_S+30)\\
&\quad [1-\exp(-[v_s+30]/9)]^{-1}\\
\beta_{mS}(v_S) &= (-3.09\times10^{-3})(v_S+30)\\
&\quad [1-\exp([v_s+30]/9)]^{-1}\\
\tau_{mS}(v_S) &= 1/(\alpha_{mS}(v_S)+\beta_{mS}(v_S)).
\end{aligned} \tag{7}$$

Table 4 M-current parameters

Parameter	Value
$g^{const}_{M2/4}$ (mS/cm^2)	0.04
θ_{mT} (mV)	− 50
σ_{mT} (mV)	5
τ_{mT} (ms)	500
$g_{M2/4max}$ (mS/cm^2)	9
θ_{gT}	9
σ_{gT}	− 0.1
τ_{gT} (ms)	500
g^{const}_{M1} (mS/cm^2)	1.3
g_{M1max} (mS/cm^2)	3
θ_{gS}	2
σ_{gS}	1.8
τ_{gS} (ms)	100

The dynamics of the M-current conductance m_S is identical to the dynamics for m_T, the corresponding conductance in the TAN. The term A_S in Eq. (7) denotes the level of ACh bound to SPN M-receptors. See Table 4 for parameter values for the M-current system.

Results

In this section, we consider the activity of our TAN model in a variety of situations motivated by published experimental observations. For a concise list of the experimental conditions reproduced and parameter changes implemented to represent these conditions, see Table 5; all other parameters were set as in Tables 1, 2.

TAN model reproduces tonic, bursting, and irregular firing modes

In spite of their name, TANs exhibit a variety of firing patterns, which we broadly characterize as tonic firing, burst firing, and irregular firing. Each firing mode also yields an associated behavior in response to the application of TTX (Wilson 2005).

In the tonic firing regime, neurons engage in tonic 4–15 Hz spiking with shallow hyperpolarizations reaching an average of voltage of − 67 mV (Bennett et al. 2000; Wilson 2005; Goldberg et al. 2009). In its tonic firing mode, our model produces a steady firing rate of about 8 Hz, with hyperpolarizations reaching − 69 mV. To achieve this firing regime, we set g_h to 1.5 mS/cm^2. In the tonic firing regime, application of TTX yields a steady voltage above firing threshold (Wilson 2005), which our model reproduces (Figs. 2, 3A). In this regime, firing is slow enough that p, the gating variable of the sag current I_h, remains relatively

Table 5 Experiments considered and associated parameter values

Experiment	Parameters	Values
TTX response (rat) (Wilson 2005)	g_{Na}, g_{NaP} and ρ_{max}	0, 0, 0
Trapezodial input (rat) (Zhang et al. 2018)	g_{Na}, g_{NaP} and ρ_{max}	0, 0, 0
Hyperpolarizing input (rat) (Choi et al. 2020)	ρ_{max}	0
Depolarizing input (rat) (Reynolds et al. 2004)	ρ_{max}	0
Apamin (rat) (Wilson 2005)	g_K and g_{mAHP}	10, 0

active, and overcomes the hyperpolarizing effects of the M-current I_M and I_{mAHP}, blocking the engagement of I_{IR} and thus preventing deep hyperpolarizations.

The burst firing mode is characterized by 0.5–1.5 s bursts of firing separated by deep hyperpolarizations to near the K^+ reversal potential (Wilson 2005; Goldberg and Reynolds 2011). The mechanism that allows TANs to undergo this deep, prolonged pause is thought to be important in regulating learning, as the cessation of TAN activity disinhibits dopamine terminals (Conceição et al. 2017). To put our model into bursting mode, we reduce the maximal conductance of the sag current g_h to 0.8 mS/cm^2. With g_h reduced to 0.8, the model exhibits bursting with an average firing rate of about 13Hz, with each burst cycle lasting about 650 ms, and with the deepest hyperpolarizations reaching about −85 mV. As the cell fires, the magnitude of its sag current, I_h, decays. Once I_h has decayed sufficiently, the inward rectifier current, I_{IR}, amplified by the lower potassium reversal potential, is engaged, which induces deep hyperpolarizations. In this scenario, the M-current I_M and I_{mAHP} contribute to driving voltage low enough to engage the inward rectifier I_{IR}, but are not required. At the resulting low voltages, I_h can recover, but its slow time constant delays this effect (Figs. 2B, 4). In this regime, TTX induces a slow, non-spiking oscillation with a period of up to about 2 s.

Since the I_h and I_{mAHP} currents are central to sculpting the TAN firing pattern, we examined the effects of varying the conductances of these currents in more detail. Specifically, we fixed the k_m parameter, which controls the calcium level at which I_{mAHP} achieves half activation, at several values and identified the boundary at which the cell switched from tonic firing to bursting (Fig. 5). In brief, decreasing g_h or increasing g_{mAHP} favors the dominance of I_{mAHP} over I_h, and the associated attainment of deeper, prolonged hyperpolarizations and hence promotes a transition from tonic spiking to bursting. Increasing k_m tilts the balance toward I_h, such that more extreme changes in these conductances are needed to push the neuron out of the tonic spiking regime.

Interestingly, for each k_m that we explored, we found a robust regime in which the cell is bursting, but under the effects of TTX does not exhibit subthreshold oscillations, and the existence of such a regime represents a prediction of our model. In this regime, the activity of I_{mAHP} during spiking provides sufficient hyperpolarization to engage the inward rectifier current, causing the cell to exhibit a deep hyperpolarization. In the absence of spiking, however, I_h remains strong enough to prevent I_{IR} from initiating the subthreshold oscillatory activity, so the cell remains at a steady voltage level.

Separately, we also find that reduction of the baseline potassium concentration parameter K_{base} to 3.7 mM may induce bursting. This change has a global effect on all potassium currents, but in particular, it alters the current–voltage relation for I_{IR}, favoring its activation to levels that can overtake I_h. Although this K_{base} is inconsistent with experimental slice preparations, changes in this concentration may represent an alternative mechanism that could yield TAN bursting in vivo. There, variability in the baseline potassium concentration could result from various effects including differences in activity of other local neurons, changes in vascular properties, or neuromodulation (Moghaddam and Adams 1987; Amédée et al. 1997; Hemond et al. 2008).

Irregular firing can be viewed as a mixture of the previous two regimes, featuring slow firing separated by both shallow and deep hyperpolarizations, as well as large subthreshold oscillations without firing. The deep hyperpolarizations in this regime in our model reach about −80 mV, consistent with experimental recordings (Wilson 2005; Goldberg and Reynolds 2011). While the firing in this regime in our deterministic model is periodic, we do obtain large subthreshold excursions as part of the periodic pattern, and inclusion of a small amplitude noise term recovers the more irregular characteristic of this firing pattern observed experimentally (Figs. 2, 3C). TTX causes slow oscillations in the irregular firing mode, which are shallower and faster than in the bursting case (Wilson 2005; Goldberg and Reynolds 2011) (Figs. 2, 3C).

Since TANs are most known for their tonic behavior, we next validated our TAN model by testing the ability of the model, with the parameter values associated with the tonic firing regime, to reproduce four benchmarks derived from experimental observations, beyond its basic firing pattern and behavior under TTX. This step provided much more rigorous constraints on the model parameter values than those resulting from simply matching the tonic firing pattern alone.

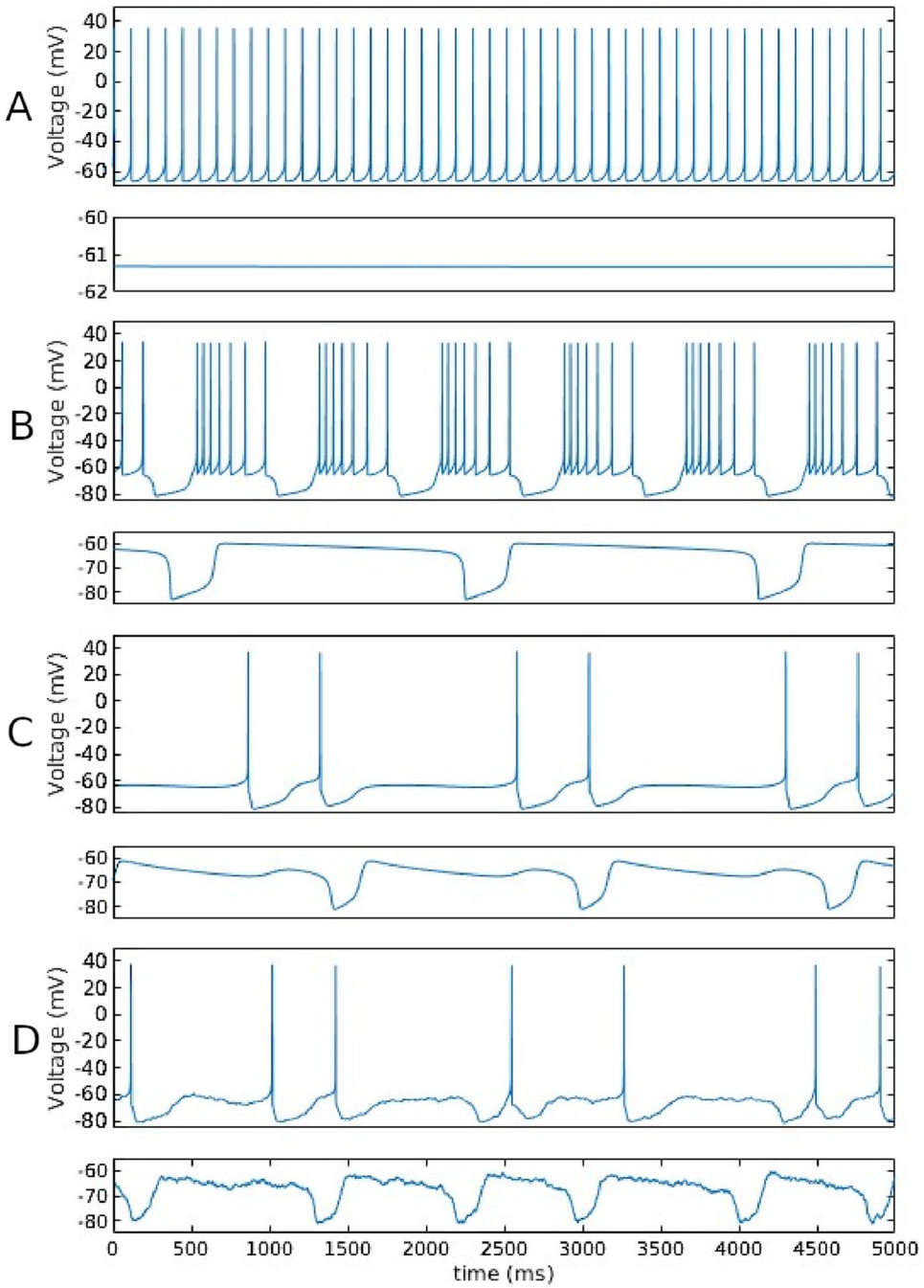

Fig. 2 Simulated TAN firing modes and responses to TTX. **A** Tonic firing. Upper: The cell fires at a steady rate of about 8 Hz. The hyperpolarization is shallow. Lower: TTX suppresses firing, and the cell remains at a steady voltage of −60 mV. **B** Bursting. Upper: The cell exhibits periods of rapid firing, punctuated by quiescence. Lower: Under TTX, the cell engages in slow oscillations featuring deep hyperpolarizations. **C** Irregular firing. Upper: The cell exhibits both shallow and deep hyperpolarizations. Overall, the firing rate is much lower than in the other modes, and there are epochs where action potentials fail to materialize. Lower: Under TTX, slow, regular oscillations occur, although they are faster and shallower than the bursting case. **D** Irregular firing with noise. With noise added, the irregularity of the spiking is more pronounced. Note that in all simulations, the total duration is 5 s, which is longer than the length of the time bar in the experimental traces in Fig. 3

Trapezoidal input current captures undershoot following gradual removal of input current

Zhang et al. (2018) found that the voltage time course of a TAN given a trapezoidal input current after TTX application exhibits a characteristic form. Of particular note is the "undershoot" effect following the removal of input, where the voltage of the cell falls below its baseline level, which helps to expose the time courses of subthreshold currents that are thought to be important in generating TAN pauses. Our model matches the following qualitative features when stimulated with a trapezoidal current I_{app} under TTX (Fig. 6): A concave rise in voltage, a small voltage overshoot followed by a plateau when the applied current plateaus, and a deeper voltage undershoot falling below the baseline resting potential before the applied current ends, followed by a slow return to baseline. The sag current I_h is inactive at these voltages, and it appears that I_{mAHP} is responsible for the undershoot, as it has not returned to its baseline level by the end of the input current (Fig. 6C). Due to the lack of spiking-related calcium influx, however, these

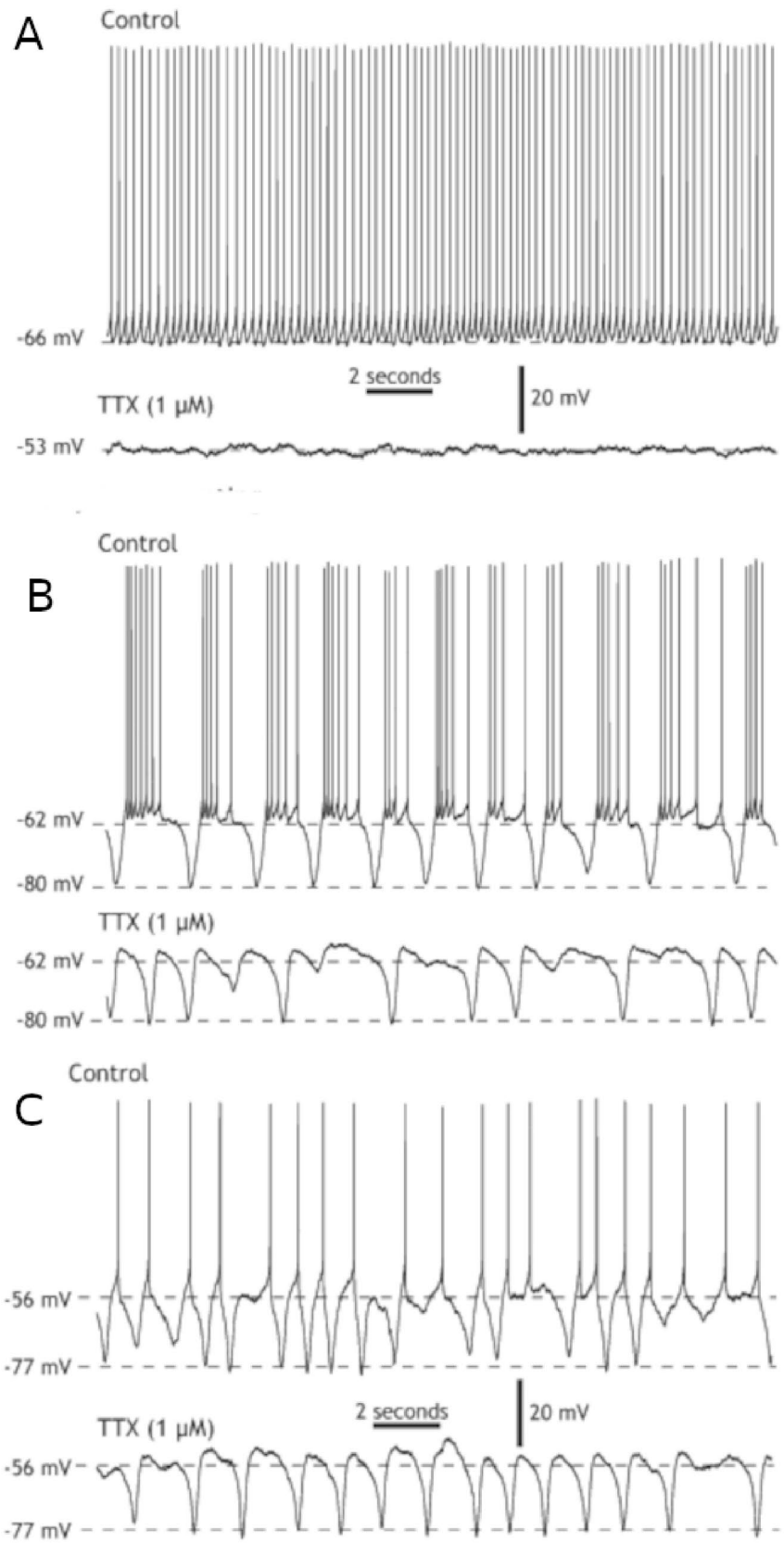

Fig. 3 Experimentally observed TAN firing modes and responses to TTX. **A** Tonic firing. Tonic firing with and without TTX. **B** Burst firing. Burst firing with and without TTX. **C** Irregular firing. Irregular firing with and without TTX. Reproduced from Wilson (2005)

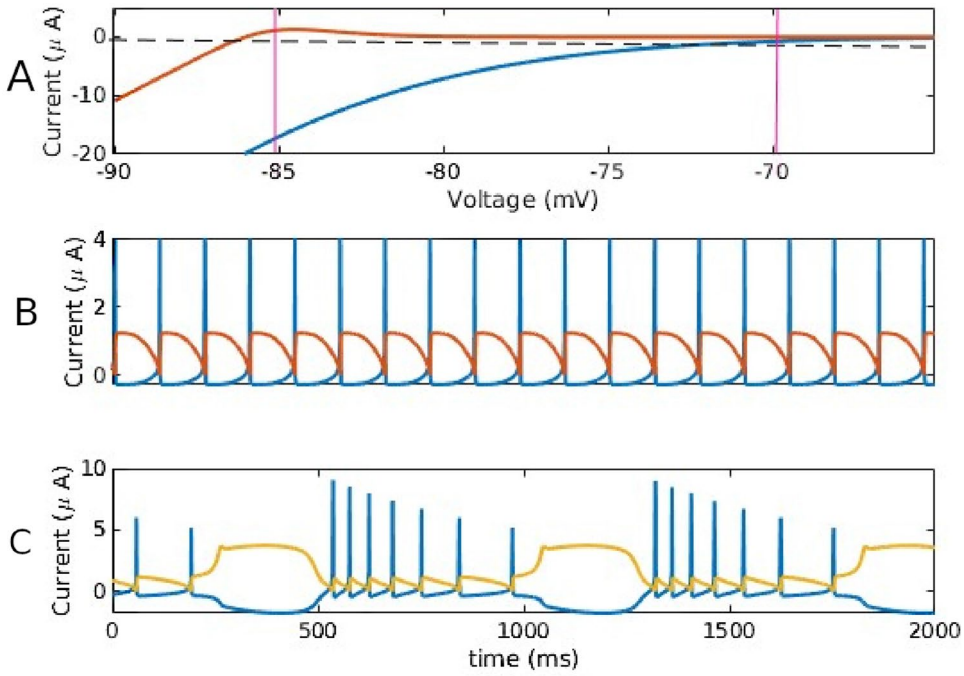

Fig. 4 IR and sag currents. **A** Steady-state values of the sag current I_h (blue) and inward rectifier current I_{IR} (orange) when voltage is clamped to various levels. Magenta (left) and purple (right) vertical lines indicate the voltages of the deepest hyperpolarizations occurring in bursting and tonic firing, respectively. **B** Time courses of I_h (blue) and I_{IR} (orange) in tonic firing. **C** Time courses of I_h (blue) and I_{IR} (yellow) currents during bursting. Negative sag currents help depolarize the membrane potential from a hyperpolarized state. In **B** and **C**, the spikes in I_h correspond to voltage spikes, while the periods of elevated I_{IR} correspond to epochs of lower voltage between spikes or bursts of spikes. Note the expanded range of the vertical axis in **C** relative to **B**

currents are not strong enough to cause the degree of hyperpolarization needed to engage the inward rectifier I_{IR}, and thus, the undershoot remains limited relative to the deeper pauses that occur after bursts.

Sag inactivation and hyperpolarization show voltage recovery

Experimental results suggest that the sag current I_h plays an important role in allowing the cell to maintain tonic firing by preventing the engagement of I_{IR} (Zhang et al. 2018; Choi et al. 2020), and we observed similar effects in our simulations (Fig. 2). If a TAN is supplied with a sufficiently hyperpolarizing applied current, then its firing ceases and its voltage remains hyperpolarized until the current is removed. However, after an initial deep hyperpolarization, there is a partial recovery of potential through the recruitment of I_h. Once the hyperpolarizing current is removed, the cell recovers to a higher firing rate than baseline, due to the deinactivation of I_{Na} that occurs during hyperpolarization. Our model captures this effect, including its dependence on the strength of the applied current I_{app} (Fig. 7).

Removal of depolarizing input generates pause with deep hyperpolarization

When a transient positive current is applied to a tonically spiking TAN, the neuron exhibits a predictable increase in firing rate. More interestingly, when this drive is removed, the TAN undergoes a deep, prolonged pause before returning to normal firing (Reynolds et al. 2004; Goldberg and Wilson 2005), and our model captures these effects (Fig. 8). In this case, while the cell is spiking, the sag current I_h decays, while the M-current I_M as well as I_{mAHP} both build up, similarly to what occurs in the burst firing mode. As with I_{mAHP} in Fig. 6, these two currents remain elevated when input is removed. This change in current balance promotes hyperpolarization, which in turn yields engagement of I_{IR}; these currents counteract the recovery of I_h and contribute to the amplitude of the hyperpolarization. I_h eventually promotes the recovery of spiking; if the experiment is run with I_h blocked, the cell will never recover from its post-input hyperpolarization, and voltage remains at −85mV.

The pause that we obtain in simulations lasts for approximately 750 ms, which lies within the range of

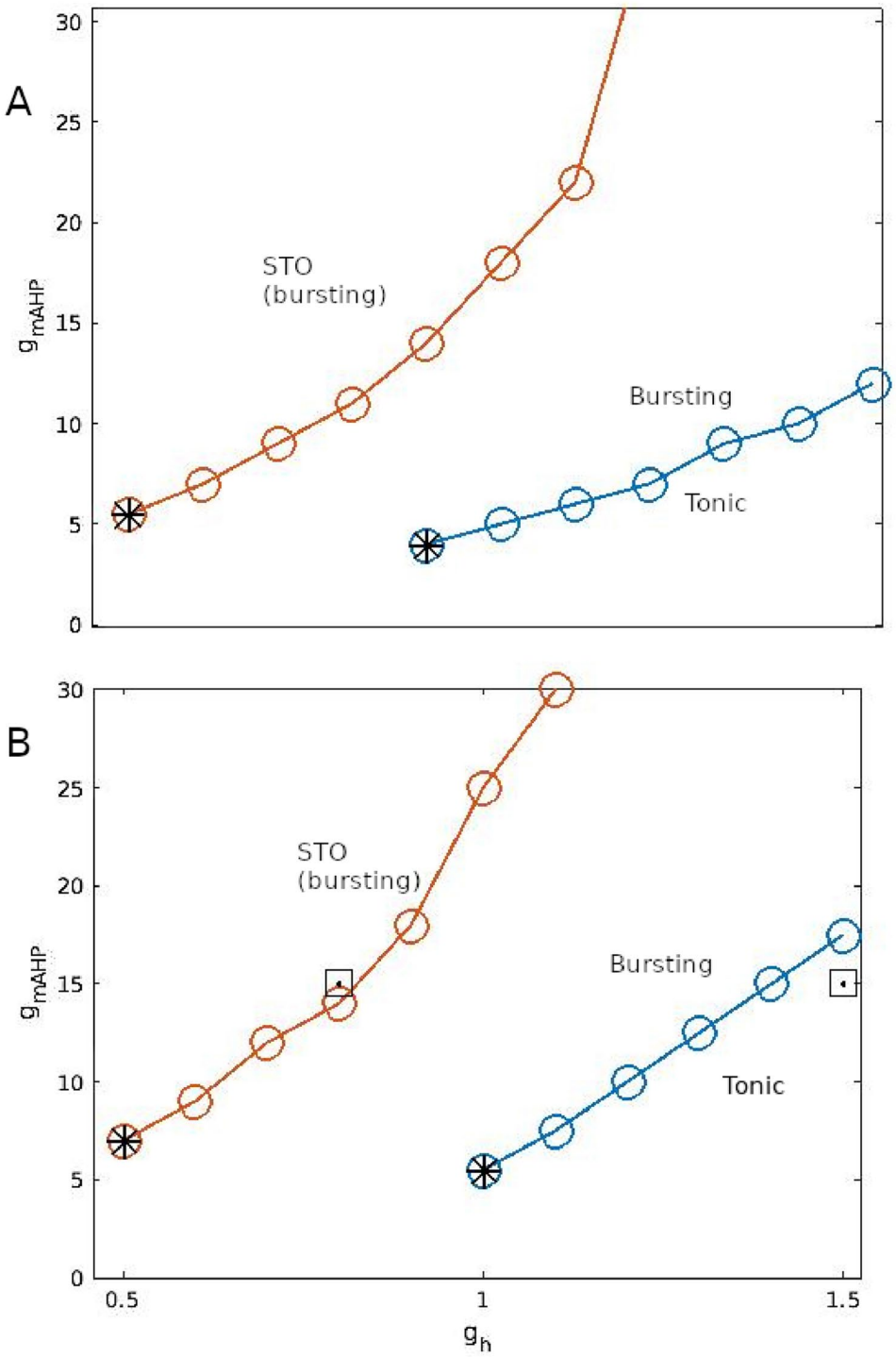

Fig. 5 Tonic and bursting parameter thresholds. The blue traces indicate the parameter values for transitions between tonic and bursting firing, while the orange traces indicate the transition between steady membrane potential and subthreshold potential oscillations under TTX for k_m values of **A** 10, and **B** 15. Values between the two curves are bursting, but do not show subthreshold oscillations under TTX. Stars indicate that g_h values below this point do not allow for tonic spiking (blue curve) or subthreshold oscillations under TTX (orange curve), respectively. The dots inside square boxes in panel **B** indicate values used for tonic and bursting simulations in Fig. 2

390–1400 ms reported in experiments (Reynolds et al. 2004; Wilson and Goldberg 2006). The pause here outlasts those seen in regular bursting, because the supplied depolarization allows hyperpolarizing currents to build up more than in the bursting setting, extending the decay time. This duration is controllable through τ_p, the membrane time constant of I_h, and ϵ, the time constant of $[Ca^{2+}]$.

Apamin causes atypical bursting

When apamin is applied to a TAN in tonic firing mode, the neuron engages in short bursts with very rapid firing, followed by deep hyperpolarizations, due to I_{sAHP} (Wilson and Goldberg 2006). To simulate apamin, we block I_{mAHP}, and our model exhibits the experimentally observed firing pattern. The new pattern results because

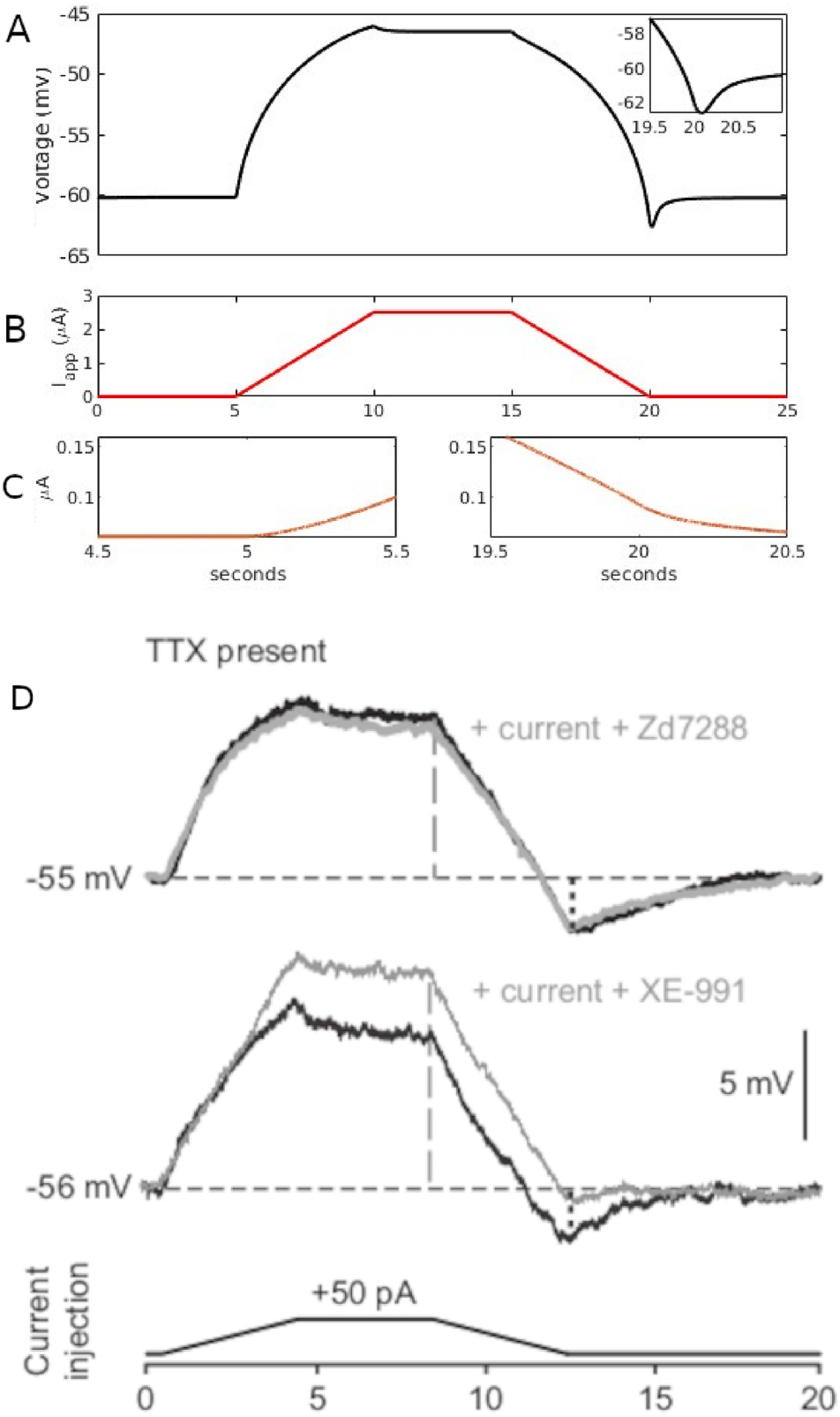

Fig. 6 Trapezoidal input: Upper: behavior of the model TAN under TTX. **A** Voltage time course in response to the application of input (**B**) shows a slight overshoot followed by a plateau. A significant undershoot occurs as input is removed, with the cell falling below baseline voltage prior to the complete removal of input. Inset in A: a closer view of the undershoot. **C** I_{mAHP} current early and late, respectively, in the response time course. Its slow decay is responsible for the voltage undershoot. **D** Experimentally recorded TAN responses to trapezoidal current injection (bottom) under TTX. Grey traces are experiments with I_h blocker Zd7288 (top) and *Kv*7.2/7.3 blocker XE-991 (middle). Panel **D** reproduced from Zhang et al. (2018)

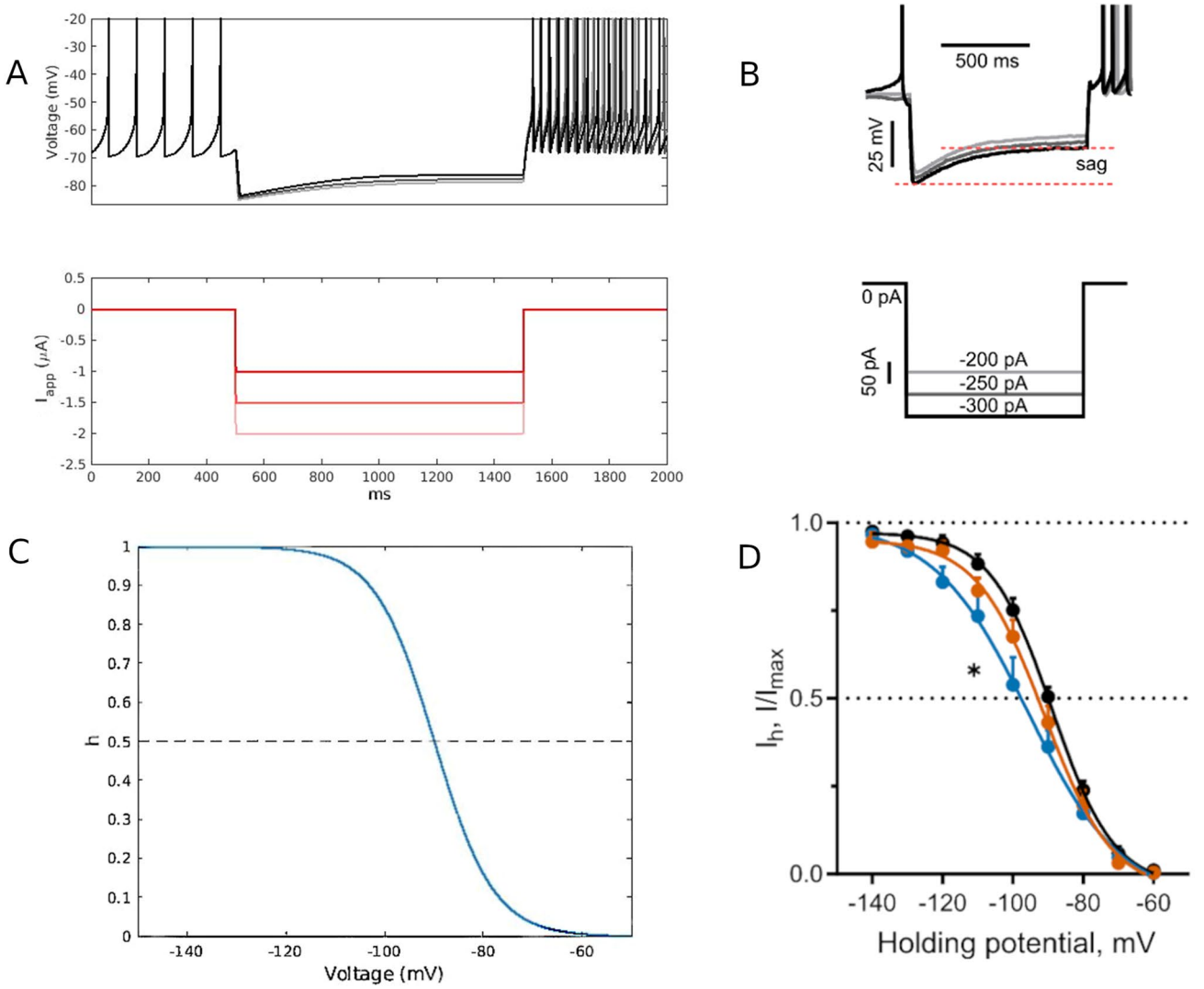

Fig. 7 Application of hyperpolarizing input reveals the sag current, I_h. **A** Model cell voltage traces (upper) in response to hyperpolarizing currents I_{app} of various levels (lower). Note the slow recovery after the initial hyperpolarization and the accelerated spiking after removal of the input. **B** Experimental hyperpolarization and sag current in response to hyperpolarizing current injection (lower traces). **C** Steady-state I_h inactivation curve, p_∞(v), from our TAN model (see Eq. (2)). Note half activation $\theta_p = -90$ mV and slope σ_p=6 (Table 1). **D** Experimental measurement of sag inactivation under voltage clamp. Black curve (with half activation near −90 mV) from control mice, blue curve from mice after dopamine depletion via 6-OHDA administration, and orange curve from dopamine depleted mice receiving levodopa treatment; only the black (control) curve is relevant to our study, and it should be compared to panel **C**. Panels **B**, **D** reproduced from Figure 3C, 3F, Choi et al. (2020) eLife, published under the Creative Commons Attribution 4.0 International Public License CC BY 4.0

when apamin reduces I_{mAHP}, a speedup of firing and a corresponding buildup of calcium occur. This accumulation in turn engages the apamin-insensitive current I_{sAHP}, which brings the voltage low enough to engage I_{IR}, resulting in a deep hyperpolarization as seen in bursting (Fig. 9).

The model can be used to explore how ACh contributes to striatal surge–pause activity in response to excitatory inputs

To this point, we have presented results showing the success of our conductance-based striatal TAN model at reproducing certain experimental observations. A property of striatal TANs that is likely critical to their role in shaping the activity of other neurons is their release of ACh. Thus, as a

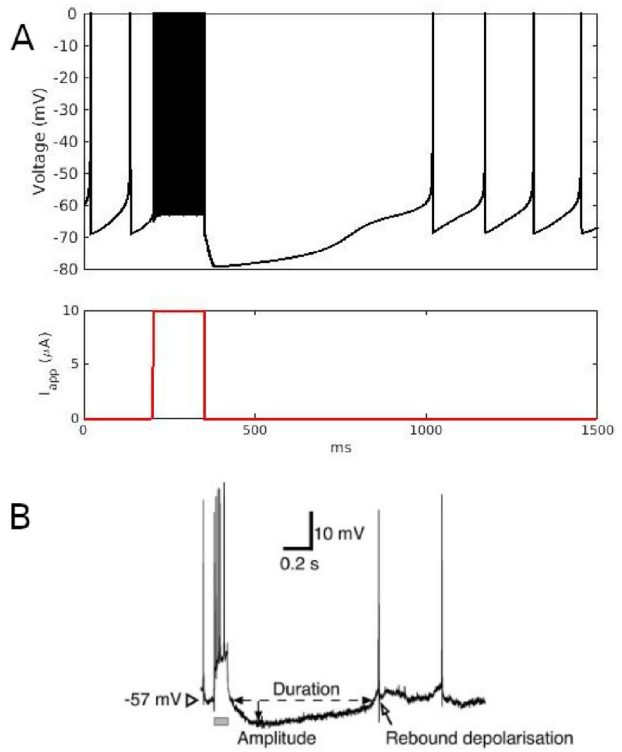

Fig. 8 Application and removal of depolarizing input current. **A** After removal of a strong, depolarizing input current, the TAN voltage undergoes a prolonged hyperpolarization and pause in spiking. **B** Experimentally recorded voltage time course corresponding to the application and removal of strong depolarizing input. Panel B reproduced from Fig. 2A Reynolds et al. (2004), Copyright 2004, Society for Neuroscience

next step, we augmented our core model to include a phenomenological but reasoned representation of the dynamics associated with the ACh released by TANs, including its impact on the M-current and on certain glutamatergic inputs to TANs (see *Materials and methods*). As an application of this addition to the model, we studied the response of the TAN model along with a previously developed SPN model (McCarthy et al. 2008) to excitatory synaptic input surges under the assumption that these cause synchronized firing of enough TANs to induce significant ACh release.

The motivation for this exploration was the experimental observation that during each motor tic induced by bicuculline application, TANs and SPNs exhibit a surge in firing, which is at least partially synchronized across neurons, followed by a prolonged pause (Fig. 10), which together have been argued to be general features of tic-associated striatal activity (Bronfeld et al. 2011; Pogorelov et al. 2015). Our working assumption is that the factor that is most likely to initiate this surge is a strong excitatory input; indeed, these striatal populations are targeted by excitatory synaptic projections from the cortex and thalamus, and similar surge and pause responses are induced by reward-related or motivationally significant stimuli (Aosaki et al. 2010; Zucca et al. 2018).

Cholinergic autoreceptors may contribute to the TAN pause after a surge of excitatory input in two primary ways. First, the enhancement of the M-current through ACh receptor activation may engage the inward rectifier current I_{IR} after the surge ends, causing the TAN to pause, while the M-current recovers, or, in the case of a prolonged surge of

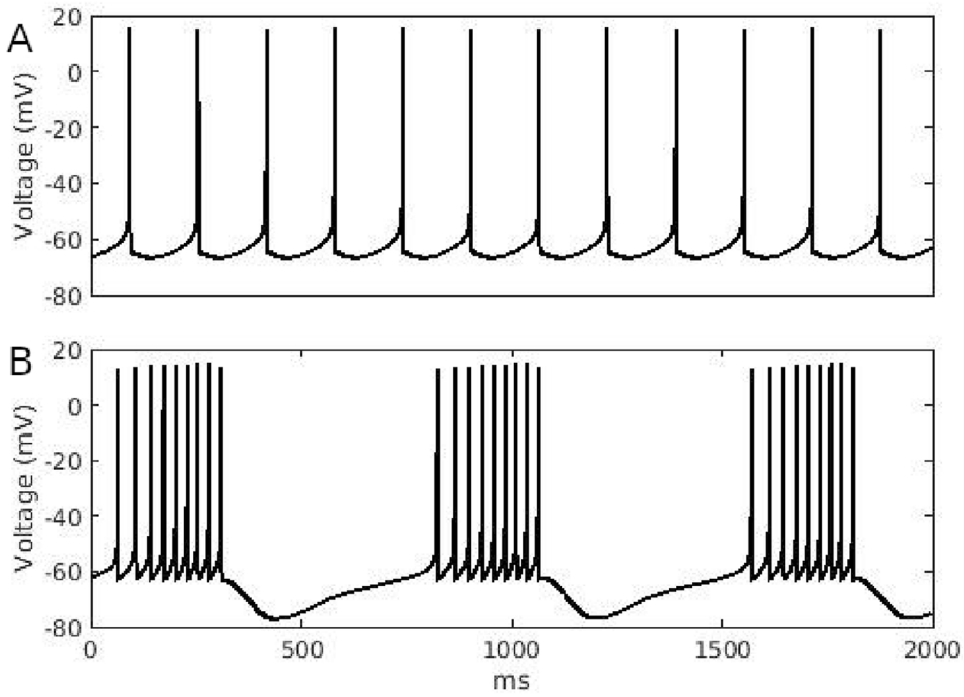

Fig. 9 Effects of apamin. **A** Tonic firing in apamin-sensitive parameter regime. **B** With the application of apamin, we see rapid spiking followed by deeper hyperpolarizations

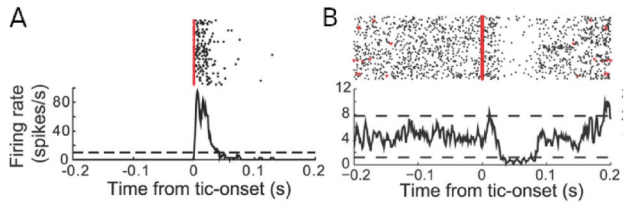

Fig. 10 Striatal activity during tic expression. Raster plot and average firing rate of **A** an SPN and **B** a TAN, across multiple motor tics induced in the presence of bicuculline. Raster plots (upper) and firing rate traces (lower) are aligned with tic onset at time 0 (red vertical lines). Reproduced from Fig. 2B, 2E, Bronfeld et al. (2011), J. Neuroscience. Published under the Creative Commons Attribution-Noncommercial-Share Alike 3.0 Unported License (CC-BY-NC-SA 3.0), doi 10.1523/JNEUROSCI.0195-11.2011

input, the enhancement of the M-current itself may overcome the excitation strongly enough to engage the inward rectifier current, while excitation is ongoing. Autoreceptors, however, do not represent the only route by which ACh impact TAN firing during an input surge. Indeed, since external projections to TAN are themselves sensitive to ACh, TANs may also modulate their own activity during an input surge indirectly by diminishing the effectiveness of the excitatory projections they receive. Here, we try to separate the impact of intrinsic (autoreceptor) and extrinsic (modulation of input current) effects of ACh on TANs, and explore the effects of different forms of TAN activity expression on SPN activity during these firing events induced by excitatory input.

In our simulations, the initial surge in TAN activity induced by excitatory input leads to a rise in ACh, which causes (see Eq. (5)) the SPN M-current conductance g_{M1} to decrease, promoting SPN firing. ACh has opposite effects on $M1$ versus $M2$ and $M4$ receptors. Thus, the rising ACh causes the TAN M-current conductance $g_{M2/4}$ to *increase*, which may initiate a TAN pause. When the pause occurs, ACh decays below its baseline level, causing g_{M1} to rise and $g_{M2/4}$ to fall. High g_{M1} may suppress SPN firing, even if some sustained excitatory input to the SPN is present. At the same time, if the TAN is in a pause phase, then the low $g_{M2/4}$ does not cause TAN activity to immediately resume. Overall, the response of the SPN to excitatory input is strongly impacted by the response of the TAN, and both are affected by the ACh profile that emerges.

We now analyze these dynamics under certain input profiles. Specifically, we assume that the rate of excitatory synaptic inputs to TANs and SPNs is either sustained, which we call the boxcar case, or linearly adapting, which we call the ramping case, since these are common cortical firing patterns.

Boxcar inputs generate surge–pause responses

In the boxcar input profile that we use, the firing rate of the input spike train jumps abruptly at onset time t_0 to 80 Hz and then jumps back to 0 abruptly at a specified offset time $t_f = t_0 + \Delta_B$ ms, with $\Delta_B = 250$ ms chosen to be longer than the TAN surges observed in the context of sensory stimuli (Aosaki et al. 2010) or motor tic production (Bronfeld et al. 2011); this choice allows us to test whether ACh effects alone can be responsible for the termination of TAN firing and subsequent pause. We allow for an input component that we call "ACh-sensitive", in reference to the fact that the effective input strength is modulated by ACh (see *Materials and methods*, Eqs. (6), (4)), which weakens the effective current felt by the postsynaptic neuron, and a component that we call "ACh-insensitive", which has a strength that is not modulated by ACh. In each case, the binding of ACh to $M_{2/4}$ receptors in the model TAN, represented by A_T, increases the TAN M-current conductance, suppressing firing and allowing for the TAN pause despite continued excitation (Figs. 11A, 12A, B). ACh also weakens the conductance of the ACh-sensitive part of the input, allowing the pause to begin before the input terminates (with similar results for longer inputs; data not shown). The pause induced by the M-current yields recruitment of the inward rectifier current, such that a significant hyperpolarization occurs during the pause, as seen experimentally (e.g., Fig. 10B). Once the TAN enters its pause phase, ACh decays and input may recover. In the ACh-insensitive case, the initial surge is more intense, leading to a greater buildup of ACh, which extends the pause duration, apparently in excess of those seen experimentally (Fig. 10), via a stronger M-current (Fig. 12B). More generally, the relative balance of ACh-sensitive and ACh-insensitive inputs tunes the pause duration between the purely sensitive and purely insensitive extremes, while shortening the length of the boxcar input can yield a failure to pause, as the firing induced by the input is not fast or sustained enough to cause sufficient decay in the sag current I_h and ACh-induced recruitment of the M-current I_M to engage the inward rectifier current I_{IR}.

Ramping inputs lead to bursting TAN activity

Since neuronal firing often features spike frequency adaptation, as an alternative to the boxcar input current, we investigate a ramping input for which the maximal input rate decays gradually over 2000 ms from the initial frequency of 80 Hz. For concreteness, we assume that after an abrupt initial jump to a maximum, the input firing rate decays linearly. As with the boxcar profile, we compare outcomes obtained when input is either ACh-sensitive or ACh-insensitive. As in the boxcar case, the initial input causes a TAN surge and, due to the ACh buildup associated with the surge, the $M_{2/4}$

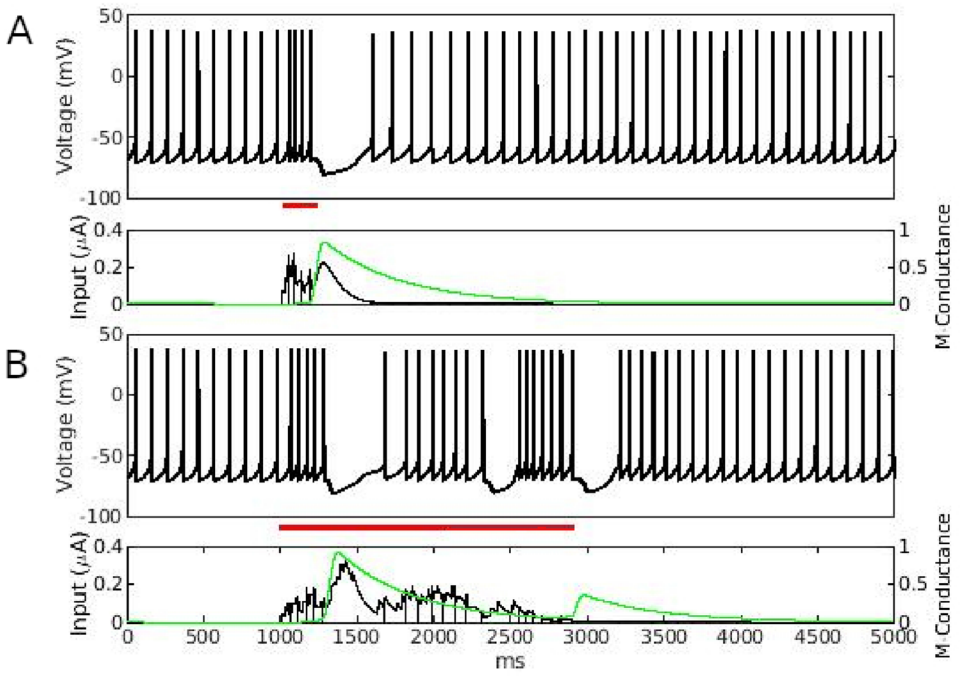

Fig. 11 Voltage traces of TAN responses to ACh-sensitive inputs. Upper plots: voltage traces. Lower plots: synaptic input current (black) and M-current conductance (green). Red bars indicate presence of spiking input. **A** Boxcar input leads to a single surge and pause. **B** With ramping input, despite some input suppression due to ACh, the input remains sufficient to cause secondary surges, which result in corresponding pauses due to cholinergic effects on the M-current

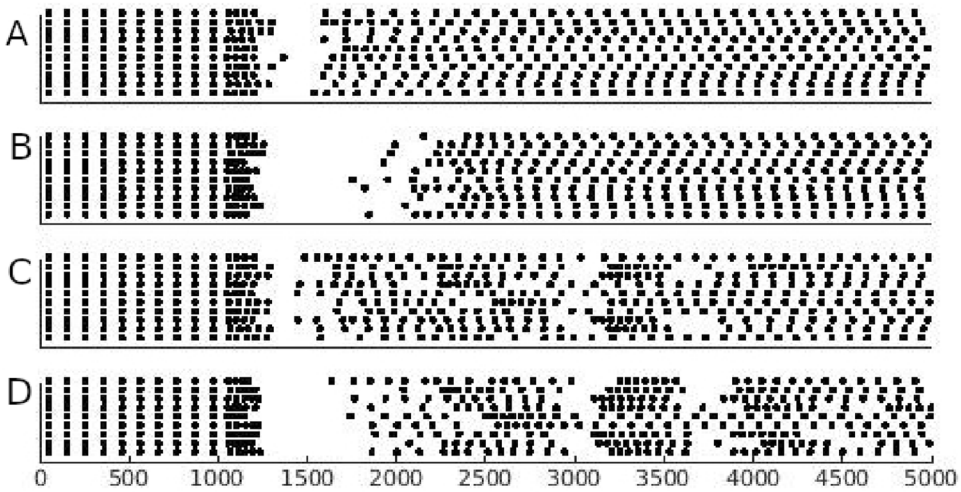

Fig. 12 Raster plots of model TAN neuron responses to inputs. **A**, **B** ACh-sensitive and -insensitive boxcar inputs, respectively, yield a surge followed by a pause. Note the more intense surging and longer pause in the ACh-insensitive case. **C**, **D** ACh-sensitive and -insensitive ramping inputs, respectively, often yield bursting epochs

receptors of the TAN can recruit the M-current and induce a pause.

In both the ACh-sensitive and ACh-insensitive cases, the continued excitatory input—which, despite the ramp, exhibits a peak in magnitude during the TAN pause due to the its restoring force at hyperpolarized voltage—reduces the duration of the TAN pause, and TAN firing resumes before the ACh has decayed to its baseline level, causing an additional increase in the ACh level. Taken together, these effects can cause the TAN to exhibit a succession of bursts and pauses as the ACh influence on the remaining input and the M-current, together with these currents' competing impacts on TAN firing, yield a feedback loop that alternately promotes and suppresses firing (Figs. 11B, 12C, D).

SPN responses to excitatory inputs are impacted by TAN activity via ACh

We next consider the firing profile of a model SPN subject to similar inputs as the TAN and also impacted by the ACh profile generated by the TAN response. Experiments show that during tic expression, SPNs produce a surge in firing and then return to their very low baseline firing rate (Bronfeld et al. (2011); Fig. 10). The model SPN is tuned, so that with its baseline input and maximal M-conductance, it fires at roughly 0.25Hz, with a rate that increases with the application of excitatory drive. The SPN neuron has no intrinsic mechanism to suppress a surge in firing in the presence of sustained excitation. Thus, its surge must end entirely due to changes in inputs or through effects of ACh release by the model TAN.

M_1-type receptors on the SPN lead to M-current reduction that facilitates firing in the presence of ACh, unlike the $M_{2/4}$ receptors found in TANs, so in our model, the maximal conductance of the SPN M-current g_{M1} decreases in the presence of ACh and rises in its absence (Eq. (5)). In our simulations, as the TAN begins a surge in firing, ACh rises and suppresses g_{M1}. Thus, I_{MS} is reduced, which enhances SPN firing above the level resulting from the input alone and contributes to the SPN surge. Once the TAN pauses, ACh decays, and if it decays below its baseline level, then A_S, and therefore, g_{M1} and I_{MS}, will rise and fight against SPN firing. As TANs return to their baseline firing rate, ACh

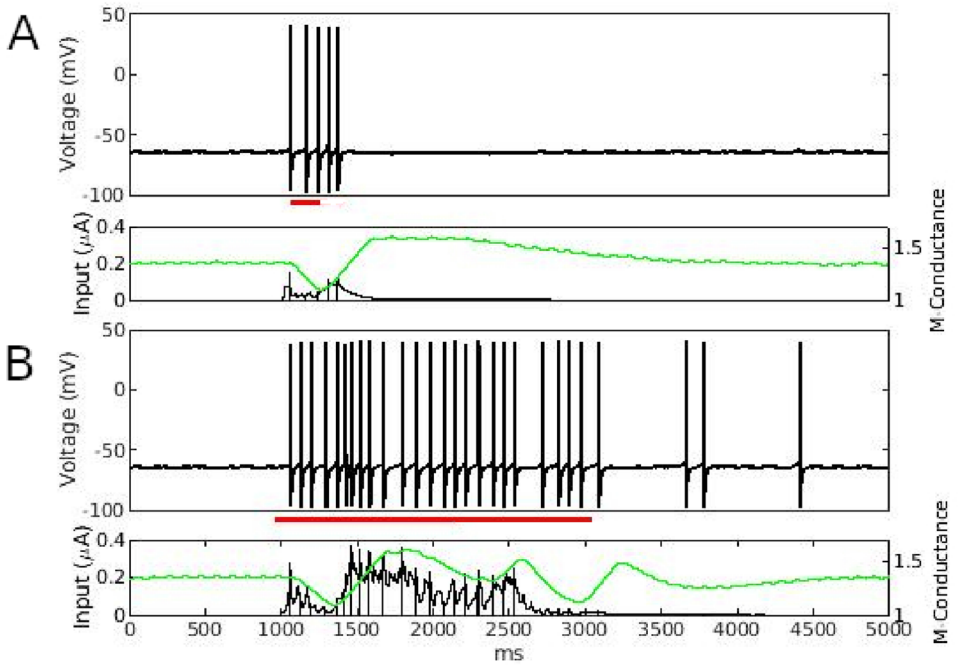

Fig. 13 Voltage traces of SPN responses to ACh-sensitive inputs. Upper plots: voltage traces. Lower plots: input current (black) and M-current conductance (green). Red bars indicate presence of spiking input **A** Boxcar input yields a transient surge in spiking. **B** Ramp input yields sustained SPN firing. Notice the correlation of input strength and M-current conductance, which are both high when ACh from the TAN is low

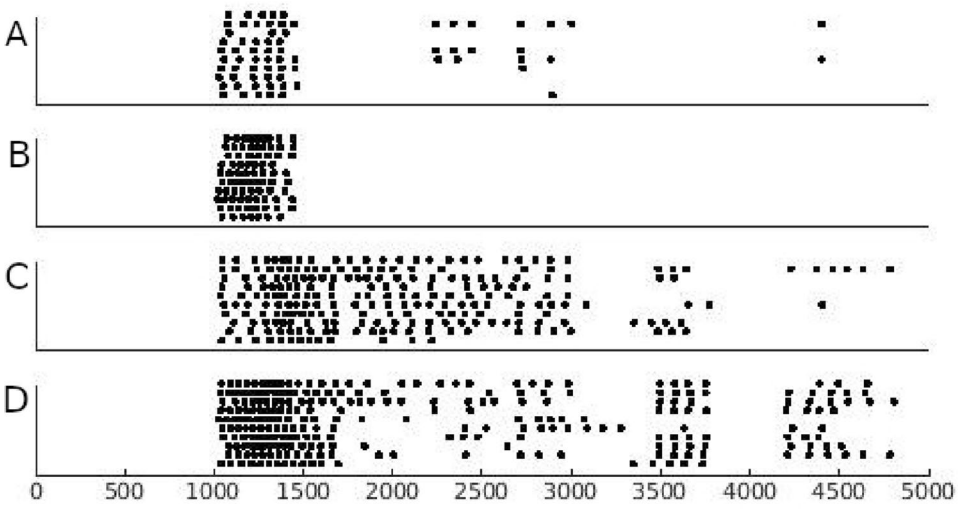

Fig. 14 Raster plots of model SPN neuron responses to inputs. **A**, **B** ACh-sensitive and -insensitive boxcar inputs, respectively, yield a surge and return to the SPN's very low baseline firing rate. **C**, **D** ACh-sensitive and -insensitive ramp inputs, respectively, yield sustained elevated firing

and g_{M1} recover to their baseline levels. We find that for boxcar inputs, the TAN pause duration induces a sufficient ACh decay to increase g_{M1}, which can overcome residual input to the SPN and shut off SPN firing (Figs. 13A; 14A, B). On the other hand, ramping inputs result in inappropriate SPN dynamics (Figs. 13B; 14C, D). For these cases, a failure in the termination of the SPN surge occurs for two primary reasons: First, the decay of ACh during the TAN pause allows the effective input to the TAN (through g_{excT}) to recover, shortening the duration of the pause. This shortened pause causes TAN firing to resume, so ACh does not decay as deeply; thus, g_{M1} does not grow much above its baseline level, and hence, I_M only weakly counters firing in the SPN. Second, TAN firing after the pause can resume at a higher rate than in baseline conditions (Fig. 12C, D), such that ACh again rises above baseline, causing a decrease in g_{M1}, which contributes to a prolonged surge of SPN spiking. TANs then enter a period of bursting, and the SPN M-current conductance oscillates around its baseline level, causing SPN firing to be alternately promoted by reduced M-current conductance (when ACh is elevated) and by excitatory input (when ACh is reduced).

Discussion

We have constructed a conductance-based model of a striatal TAN that can produce various TAN spiking patterns observed experimentally and responds appropriately when tested under a wide range of conditions previously explored experimentally (Reynolds et al. 2004; Wilson 2005; Wilson and Goldberg 2006; Bronfeld et al. 2011; Zhang et al. 2018; Choi et al. 2020). To our knowledge, what we present here is the first spiking, conductance-based model of a TAN that reproduces at least qualitatively the variety of experimental benchmarks that we have considered. While a few other models of TANs exist (Wilson 2005; Tan and Bullock 2008; Franklin and Frank 2015; Zhang et al. 2018; Frost Nylén et al. 2021), they are generally non-spiking models of subthreshold dynamics or otherwise unsuitable or inefficient for investigating these phenomena. Our model development therefore represents an important step forward in efforts to simulate and model striatal activity, which may be of use in studying learning and movement disorders, and allows us to predict how various currents, notably I_h, I_{IR}, and I_M, contribute to the observed TAN dynamics.

Basic model dynamics

TANs exhibit a variety of firing modes (Wilson 2005), which we can reproduce with a single model. To capture the transition between tonic spiking and bursting, we changed the conductance of I_h (see Table 1, Fig. 5) and we could also switch between spiking and bursting by tuning the calcium-sensitivity and conductance of I_{mAHP} (k_m and g_{mAHP}, Fig. 5). This parameter variation likely reflects the biological reality; that is, the differences in activity observed experimentally when TTX is applied to TANs engaged in these behaviors likely indicates that the internal mechanisms of the cells truly are tuned differently across these regimes, and hence, a small change in parameter values (here, two parameters) to switch between them is justified. Correspondingly, our model yields predictions about how pharmacologically introduced changes in the conductances of burst-related currents such as I_h, I_{mAHP} would alter TAN activity. We also predict the existence of a bursting regime in which subthreshold oscillations (STOs) would not occur (or at least would not occur on every cycle in a noisy environment) under TTX administration, as an intermediate state between tonic spiking and bursting for which TTX exposes these STOs. On the other hand, there is a possibility that there is a form of bistability between tonic spiking and bursting in TANs that our model tuning does not capture, and experiments can help distinguish between these two alternatives. Importantly, we do not shift parameter values away from our baseline tonic spiking regime when we demonstrate model agreement with experimental benchmarks except for those associated with apamin application (Fig. 9).

We additionally found that the bursting-tonic transition can occur with only a change to extracellular K^+ concentration, possibly representing an additional mechanism by which bursting can occur that has not yet been explored experimentally. This concentration is believed to exhibit local variations in vivo (Moghaddam and Adams 1987; Amédée et al. 1997; Hemond et al. 2008), and our model predicts that it could be used experimentally to modulate TAN firing between tonic spiking and bursting. Interestingly, a diversity of firing modes is also found in certain neurons in other brain areas and may also be associated with differences in potassium conductances (Hemond et al. 2008).

The tonic firing mode appears to be the TAN activity pattern most commonly observed experimentally and gives the cell its name, so we make the natural choice of selecting it as a baseline condition for our emulation of other experimental benchmarks. More work should be done in the future to consider how all of the different TAN firing modes impact TAN computation and what role they play in maintaining striatal function. Models that exhibit transitions between intrinsic activity patterns under parameter variations commonly also produce more complicated, possibly chaotic activity during these transitions (cf. Wang and Rubin (2020); Codianni (2021), although many other examples exist). Presumably neurons can also produce such intermediate activity patterns, although the details might be altered in the noisy in vivo environment and their functional significance would be

uncertain, and such activity could be compared to the model as a future test of model validity.

Effects related to ACh

We find that ACh-sensitive M-current conductances that respond to varying ACh levels represent a viable mechanism for TAN autoregulation, which has long been believed to play a role in modulating striatal function (Surmeier et al. 1996; Calabresi et al. 2000). In our model, this cholinergic modulation can yield surge–pause behavior in response to certain forms of excitatory input to TANs that induce a surge in ACh release, and this pattern resembles observations associated with motor tics induced by bicuculline administration (Bronfeld et al. 2011). Thus, our model predicts that disruptions in ACh release and effects on the M-current would interfere with pauses in TAN activity during periods of sustained input.

ACh levels have been shown to exhibit sensitivity to TAN spike patterns, suggesting that they feature relatively fast kinetics (Nosaka and Wickens 2022). Because the effects of ACh on muscarinic receptors have not been quantified precisely, however, we used a phenomenological approach to model the ACh subsystem; more precise modeling represents a natural future direction that can be pursued once further research into the precise effects associated with ACh has been conducted. The results that we have obtained with this approach may provide constraints on the time course of inputs to TANs during motor tics. Specifically, our results predict that inputs underlying surge–pause patterns of TAN activity are transient events of constrained duration, outlasting firing surges but not lasting long enough to cause rebound spikes after ACh levels recover during subsequent pauses. A caveat to this work is that, lacking data on the profiles of excitatory inputs to striatum during motor tic production, we explored two natural choices; however, it is still possible that some more complicated pattern of inputs occurs and results in the motor tic response, or that differences in cortical and thalamic input timing, which we have not considered, could contribute. Importantly, we omitted inhibition (e.g., from FSIs and other striatal interneurons) in our simulation of surge–pause profiles in TANs and SPNs, because the motor tic model in which these profiles arise is generated by local bicuculline, which implies that inhibition is not necessary for this form of dynamics; nonetheless, inhibition could shape activity in other contexts featuring TAN surge–pauses.

Roles of ionic currents in shaping TAN activity, and associated predictions

The model that we have produced is complex and hence includes many parameters, selected based on their inclusion or characterization in the past literature (see subsection "Overview of Model Components" in *Materials and methods*) and their relevance to the experiments that we describe in this work. Because we have used the model to investigate a variety of TAN behaviors that are difficult to quantify precisely, we felt that it was not realistic to engage in a systematic sensitivity analysis or quantification of model performance. Determining what features of our model allow its dynamics to match experimentally observed effects, however, does provide predictions about the roles of specific currents in shaping TAN activity patterns. Specifically, our model predicts that the inward rectifier I_{IR} and the sag I_h currents must be appropriately tuned, so that during tonic firing, I_h remains slightly dominant, keeping the cell above its firing threshold and preventing deeper hyperpolarizations, while I_{IR} is strong enough to generate pauses when the TAN undergoes excess hyperpolarization (see also Wilson (2005)). Meanwhile, I_{IR} should become slightly dominant when a TAN engages in persistent bursting activity, forcing the cell into repeated deep hyperpolarizations. This switch in firing modes is most easily achieved through changes in the sag current maximal conductance, but other hyperpolarizing currents, including inputs from GABAergic cells, may also provide a transition mechanism. The action of I_{mAHP}, which provides the necessary hyperpolarization to engage I_{IR}, is central to this interplay. Of course, despite its complexity, our computational model necessarily omits many biological effects as well as inputs to striatum from other sources, which were not necessary for the aims of this work but may turn out to be useful to add in the future.

This distinction between shallow pauses that separate tonic spikes and deeper pauses mediated by I_{IR} that arise between spike bursts represents an important dichotomy in TAN dynamics that may be relevant to learning (Kim et al. 2019; Zhang et al. 2018). More generally, our study yields interesting insights into the interplay of ionic currents in modulating interspike dynamics of the TAN membrane potential. Indeed, while the balance of I_{IR} and I_h is important for maintaining and selecting between firing modes, it is also vital to the TAN's ability to exhibit prolonged pauses. Our results build on past work (Reynolds et al. 2004; Wilson 2005; Aosaki et al. 2010) suggesting that there are numerous mechanisms by which a pause may be initiated, as long as some hyperpolarizing current can sufficiently overcome I_h. These mechanisms include enhancement of the M-current I_M by ACh buildup, recruitment of I_{mAHP} by calcium influx, weakening of the sag current I_h through depolarization induced by excitatory input followed by subsequent input termination, and, although outside of the scope of our model, the arrival of direct GABAergic inhibition. Interestingly, our model shows that with I_{mAHP} removed by apamin application, the acceleration in TAN spiking can recruit I_{sAHP} enough to interrupt activity and initiate what becomes a prolonged

pause. As long as the inward rectifier is sufficiently engaged, it can transiently dominate the cell's voltage dynamics.

Model limitations

Although our model matches several experimental observations quantitatively, the timing of certain events in our simulations, especially during deep hyperpolarizations, is not fully consistent with experimental results. This is likely a result of using fixed membrane time constants. Allowing the membrane time constant of the sag current I_h to vary with voltage could potentially alleviate these timing differences, as the deep hyperpolarizations in the model result from an interplay between I_h and other hyperpolarizing currents (e.g., I_{IR}). Second, while the activity of our model depends on the M-current I_M, which is not completely inactive at hyperpolarized voltages, there may be additional subthreshold currents that we have not captured. For example, in the trapezoidal input experiment done by Zhang et al. (2018), as input is ramped down, the experimentally observed voltage is roughly linear, while the voltage trace of our model is concave (Fig. 6A, D). We note that in our model in the bursting regime, the subthreshold oscillations under TTX are on the long end of those observed experimentally (Wilson 2005), and these changes may alter this timing. Third, there is some subtlety missing in our representation of calcium-sensitive AHP currents. Both experimentally and in our model, an influx of calcium can cause the cell to transiently enter the bursting regime, but it is not clear from our simulations that calcium dynamics alone can sustain bursting. Moreover, our model requires some adjustment of parameter values to respond accurately to apamin, and even in the apamin-sensitive parameter regime produces hyperpolarizations slightly shallower than those seen experimentally. It may be possible to resolve these small discrepancies using a different formulation of the sAHP current or tuning of the $[Ca^{2+}]$ subsystem. Finally, the external input to TANs in our final simulations dealing with input-driven surge–pause patterns is overly generic. While we demonstrate that M-currents offer a viable mechanism for generating the motor tic response, we do not aim to dissect the precise nature of the different input signals during surge events, though this is an avenue worth investigating in the future.

Relevant literature and future directions

While our approach shows that tuning of a small set of factors suffices to modulate firing patterns in an isolated TAN neuron, it is likely that TAN activity observed in experiments is influenced by the activity of a veritable zoo of other striatal cell types, many of which have ACh-sensitive nicotinic receptors (Orth et al. 2005; Abudukeyoumu et al. 2019). Although many of these neurons are quite sparse within the striatum, these cells have recently been shown to play important roles in mediating TAN function (e.g., GABAergic NPY-NGF neurons studied in English et al. (2012); Assous et al. (2017)). Although these GABAergic inputs were not relevant for our simulations, they likely contribute to TAN responses during normal striatal function and could be modeled in future work as a step toward developing a comprehensive computational model of striatum. An important but brief recent study did use multi-compartmental models to simulate striatal TAN and low-threshold spiking (LTS) neurons with a focus on their responses to cortical and thalamic inputs (Frost Nylén et al. 2021), although that work did not consider the range of experimental conditions that we have emulated and used to constrain our model. Considering distinct effects of these two input classes in our single-compartment model, perhaps guided by the representations of these inputs and their processing by the large dendritic arbor of striatal TANs described in the multi-compartmental work, could allow for related investigations in a computationally efficient setting. More detailed models may also take into account the fact that SPNs are heterogeneous, with direct pathway SPNs specifically expressing M_4 channels (Higley et al. 2009; Kreitzer 2009) and hence potentially responding differently to ACh variations.

Dopamine is a crucial modulator of TAN behavior, which is widely believed to play an important role in the process of learning, particularly during TAN pauses (Zhou et al. 2002; Centonze et al. 2003; Morris et al. 2004; Aosaki et al. 2010; Ashby and Crossley 2011; Tan and Bullock 2008; Conceição et al. 2017; Kim et al. 2019). Indeed, motor tics may be learned responses to corticothalamic surges (Conceição et al. 2017), and the pause following TAN surges may contribute to this learning process. Despite its likely importance, the DA–TAN interaction is complex and bi-directional and has not been implicated directly in the activity patterns that we have studied, and hence, we have not modeled it in this work, leaving this as another direction for future research.

A final point worth mentioning is that we performed our model parameter tuning manually, using reasoning based on our understanding of the dynamics associated with conductance-based models. While various toolkits for parameter tuning have been published and shared online, we could not see a way to adapt them for the diverse range of experimental benchmarks, in many cases qualitative, that we sought to meet. If a suitable option or data set for automated parameter tuning of this model becomes available, then making use of such a tool could allow for a more thorough exploration of model dynamics and effects of parameter variations.

Conclusions

Ultimately, we have developed a biologically constrained model of a TAN that fits a variety of experimental observations and have used it to explore both the roles of various

currents in shaping TAN dynamics and the way that feedback effects associated with ACh contribute to TAN and SPN surge–pause responses to excitatory inputs, as may occur during motivationally relevant stimulus presentation or in motor tic production after bicuculline application. Incorporating this autoregulation into computational models including networks of striatal neurons may help to determine what functional roles different firing modes play in regulating striatal activity and in ACh–DA interactions associated with corticostriatal synaptic plasticity and learning.

Funding This work was partially supported by the NSF CRCNS under Award DMS 1724240 and the NSF under Award DMS 1951095. The authors thank Izhar Bar-Gad and Fred Hamker and their lab members for discussions related to this work.

Declarations

Data availability No original experimental data were involved in this study. Codes used for model simulations will be made publicly available at ModelDB (https://senselab.med.yale.edu/ModelDB/) upon acceptance of this work for publication.

Conflict of interest The authors declare no competing financial interests.

Significance statement Despite a growing recognition that striatal cholinergic interneurons, also known as tonically active neurons (TANs), can significantly impact synaptic plasticity and firing patterns of projection neurons in the striatum, there has been relatively little computational work to simulate and analyze their properties. We address this gap by developing a computational model of TANs, fit to match a large collection of experimental results. Simulations of the computational model allow us to analyze the roles of various transmembrane currents in producing TAN responses and the contribution of acetylcholine released by TANs in sculpting their activity in response to excitatory inputs, which could have implications for reinforcement learning and for motor tics in conditions such as Tourette's syndrome.

References

Abudukeyoumu N, Hernandez-Flores T, Garcia-Munoz M, Arbuthnott G (2019) Cholinergic modulation of striatal microcircuits. Eur J Neurosci 49(5):604–622

Amédée T, Robert A, Coles J (1997) Potassium homeostasis and glial energy metabolism. Glia 21(1):46–55

Aosaki T, Miura M, Suzuki T, Nishimura K, Masuda M (2010) Acetylcholine-dopamine balance hypothesis in the striatum: an update. Geriatr Gerontol Int 10:S148–S157

Ashby F, Crossley M (2011) A computational model of how cholinergic interneurons protect striatal-dependent learning. J Cogn Neurosci 23(6):1549–1566

Assous M, Kaminer J, Shah F, Garg A, Koós T, Tepper J (2017) Differential processing of thalamic information via distinct striatal interneuron circuits. Nat Commun 8(1):1–14

Barreto E, Cressman JR (2011) Ion concentration dynamics as a mechanism for neuronal bursting. J Biol Phys 37(3):361–373

Bennett B, Callaway J, Wilson C (2000) Intrinsic membrane properties underlying spontaneous tonic firing in neostriatal cholinergic interneurons. J Neurosci 20(22):8493–8503

Brimblecombe KR, Threlfell S, Dautan D, Kosillo P, Mena-Segovia J, Cragg SJ (2018) Targeted activation of cholinergic interneurons accounts for the modulation of dopamine by striatal nicotinic receptors. eNeuro 5(5):2

Bronfeld M, Belelovsky K, Bar-Gad I (2011) Spatial and temporal properties of tic-related neuronal activity in the cortico-basal ganglia loop. J Neurosci 31(24):8713–8721

Bronfeld M, Yael D, Belelovsky K, Bar-Gad I (2013) Motor tics evoked by striatal disinhibition in the rat. Front Syst Neurosci 7:50

Calabresi P, Centonze D, Gubellini P, Pisani A, Bernardi G (2000) Acetylcholine-mediated modulation of striatal function. Trends Neurosci 23(3):120–126

Centonze D, Gubellini P, Pisani A, Bernardi G, Calabresi P (2003) Dopamine, acetylcholine and nitric oxide systems interact to induce corticostriatal synaptic plasticity. Rev Neurosci 14(3):207–216

Choi S, Ma T, Ding Y, Cheung T, Joshi N, Sulzer D, Kang U (2020) Alterations in the intrinsic properties of striatal cholinergic interneurons after dopamine lesion and chronic l-dopa. Elife 9:e56920

Codianni M (2021) Case studies in forcing small motor neural circuits. PhD thesis, University of Pittsburgh

Conceição VA, Dias Â, Farinha AC, Maia TV (2017) Premonitory urges and tics in tourette syndrome: computational mechanisms and neural correlates. Curr Opin Neurobiol 46:187–199

Corbit V, Zitelli K, Crilly S, Rubin J, Gittis A (2016) Pallidostriatal projections promote β oscillations in a dopamine-depleted biophysical network model. J Neurosci 36(20):5556–5571

Ding J, Guzman J, Tkatch T, Chen S, Goldberg J, Ebert P, Surmeier D (2006) Rgs4-dependent attenuation of m 4 autoreceptor function in striatal cholinergic interneurons following dopamine depletion. Nat Neurosci 9(6):832–842

Ding J, Guzman J, Peterson J, Goldberg J, Surmeier D (2010) Thalamic gating of corticostriatal signaling by cholinergic interneurons. Neuron 67(2):294–307

Ding Y, Won L, Britt JP, Lim SAO, McGehee DS, Kang UJ (2011) Enhanced striatal cholinergic neuronal activity mediates l-dopa-induced dyskinesia in parkinsonian mice. Proc Natl Acad Sci 108(2):840–845

Dolezal V, Wecker L (1990) Muscarinic receptor blockade increases basal acetylcholine release from striatal slices. J Pharmacol Exp Ther 252(2):739–743

English D, Ibanez-Sandoval O, Stark E, Tecuapetla F, Buzsáki G, Deisseroth K, Koos T (2012) Gabaergic circuits mediate the reinforcement-related signals of striatal cholinergic interneurons. Nat Neurosci 15(1):123

Ermentrout B (2002) Animating dynamical systems: a guide to xppaut for researchers and students. SIAM, Philadelphia

Fink C, Booth V, Zochowski M (2011) Cellularly-driven differences in network synchronization propensity are differentially modulated by firing frequency. PLoS Comput Biol 7(5):e1002062

Fink C, Murphy G, Zochowski M, Booth V (2013) A dynamical role for acetylcholine in synaptic renormalization. PLoS Comput Biol 9(3):e1002939

Franklin N, Frank M (2015) A cholinergic feedback circuit to regulate striatal population uncertainty and optimize reinforcement learning. Elife 4:e12029

Frost Nylén J, Carannante I, Grillner S, Hellgren Kotaleski J (2021) Reciprocal interaction between striatal cholinergic and low-threshold spiking interneurons-a computational study. Eur J Neurosci 53(7):2135–2148

Gabel L, Nisenbaum E (1999) Muscarinic receptors differentially modulate the persistent potassium current in striatal spiny projection neurons. J Neurophysiol 81(3):1418–1423
Giocomo L, Hasselmo M (2007) Neuromodulation by glutamate and acetylcholine can change circuit dynamics by regulating the relative influence of afferent input and excitatory feedback. Mol Neurobiol 36(2):184–200
Goldberg J, Reynolds J (2011) Spontaneous firing and evoked pauses in the tonically active cholinergic interneurons of the striatum. Neuroscience 198:27–43
Goldberg J, Wilson C (2005) Control of spontaneous firing patterns by the selective coupling of calcium currents to calcium-activated potassium currents in striatal cholinergic interneurons. J Neurosci 25(44):10230–10238
Goldberg J, Teagarden M, Foehring R, Wilson C (2009) Nonequilibrium calcium dynamics regulate the autonomous firing pattern of rat striatal cholinergic interneurons. J Neurosci 29(26):8396–8407
Gritton H, Howe W, Romano M, DiFeliceantonio A, Kramer M, Saligrama V, Han X (2019) Unique contributions of parvalbumin and cholinergic interneurons in organizing striatal networks during movement. Nat Neurosci 22(4):586–597
Hemond P, Epstein D, Boley A, Ascoli G, Jaffe D (2008) Distinct classes of pyramidal cells exhibit mutually exclusive firing patterns in hippocampal area ca3b. Hippocampus 18(4):411–424
Higley M, Soler-Llavina G, Sabatini B (2009) Cholinergic modulation of multivesicular release regulates striatal synaptic potency and integration. Nat Neurosci 12(9):1121–1128
Howe A, Surmeier D (1995) Muscarinic receptors modulate n-, p-, and l-type ca2+ currents in rat striatal neurons through parallel pathways. J Neurosci 15(1):458–469
Ishii M, Kurachi Y (2006) Muscarinic acetylcholine receptors. Curr Pharm Des 12(28):3573–3581
Kim T, Capps R, Hamade K, Barnett W, Todorov D, Latash E, Molkov Y (2019) The functional role of striatal cholinergic interneurons in reinforcement learning from computational perspective. Front Neural Circ 13(10):2
Kondabolu K, Roberts E, Bucklin M, McCarthy M, Kopell N, Han X (2016) Striatal cholinergic interneurons generate beta and gamma oscillations in the corticostriatal circuit and produce motor deficits. Proc Natl Acad Sci 113(22):E3159–E3168
Kreitzer A (2009) Physiology and pharmacology of striatal neurons. Annu Rev Neurosci 32:127–147
Kreitzer A, Berke J (2011) Investigating striatal function through cell-type-specific manipulations. Neuroscience 198:19–26
Krishnan G, Chauvette S, Shamie I, Soltani S, Timofeev I, Cash S, Bazhenov M (2016) Cellular and neurochemical basis of sleep stages in the thalamocortical network. Elife 5:e18607
Lim SAO, Xia R, Ding Y, Won L, Ray WJ, Hitchcock SA, McGehee DS, Kang UJ (2015) Enhanced histamine h2 excitation of striatal cholinergic interneurons in l-dopa-induced dyskinesia. Neurobiol Dis 76:67–76
Maurice N, Mercer J, Chan C, Hernandez-Lopez S, Held J, Tkatch T, Surmeier D (2004) D2 dopamine receptor-mediated modulation of voltage-dependent na+ channels reduces autonomous activity in striatal cholinergic interneurons. J Neurosci 24(46):10289–10301
McCarthy M, Brown E, Kopell N (2008) Potential network mechanisms mediating electroencephalographic beta rhythm changes during propofol-induced paradoxical excitation. J Neurosci 28(50):13488–13504
McCarthy M, Moore-Kochlacs C, Gu X, Boyden E, Han X, Kopell N (2011) Striatal origin of the pathologic beta oscillations in parkinson's disease. Proc Natl Acad Sci 108(28):11620–11625
McKinley J, Shi Z, Kawikova I, Hur M, Bamford I, Devi S, Bamford N (2019) Dopamine deficiency reduces striatal cholinergic interneuron function in models of parkinson's disease. Neuron 103(6):1056–1072
Moehle M, Conn P (2019) Roles of the m4 acetylcholine receptor in the basal ganglia and the treatment of movement disorders. Mov Disord 34(8):1089–1099
Moghaddam B, Adams R (1987) Regional differences in resting extracellular potassium levels of rat brain. Brain Res 406(1–2):337–340
Morris G, Arkadir D, Nevet A, Vaadia E, Bergman H (2004) Coincident but distinct messages of midbrain dopamine and striatal tonically active neurons. Neuron 43(1):133–143
Nisenbaum E, Wilson C, Foehring R, Surmeier D (1996) Isolation and characterization of a persistent potassium current in neostriatal neurons. J Neurophysiol 76(2):1180–1194
Nosaka D, Wickens J (2022) Striatal cholinergic signaling in time and space. Molecules 27(4):1202
Orth M, Amann B, Robertson M, Rothwell J (2005) Excitability of motor cortex inhibitory circuits in tourette syndrome before and after single dose nicotine. Brain 128(6):1292–1300
Pakhotin P, Bracci E (2007) Cholinergic interneurons control the excitatory input to the striatum. J Neurosci 27(2):391–400
Perez-Lloret S, Barrantes FJ (2016) Deficits in cholinergic neurotransmission and their clinical correlates in parkinson's disease. NPJ Parkinson's Dis 2(1):1–12
Pisani A, Bernardi G, Ding J, Surmeier D (2007) Re-emergence of striatal cholinergic interneurons in movement disorders. Trends Neurosci 30(10):545–553
Pogorelov V, Xu M, Smith H, Buchanan G, Pittenger C (2015) Corticostriatal interactions in the generation of tic-like behaviors after local striatal disinhibition. Exp Neurol 265:122–128
Reynolds J, Hyland B, Wickens J (2004) Modulation of an afterhyperpolarization by the substantia nigra induces pauses in the tonic firing of striatal cholinergic interneurons. J Neurosci 24(44):9870–9877
Shen W, Hamilton S, Nathanson N, Surmeier D (2005) Cholinergic suppression of kcnq channel currents enhances excitability of striatal medium spiny neurons. J Neurosci 25(32):7449–7458
Song W, Tkatch T, Baranauskas G, Ichinohe N, Kitai S, Surmeier D (1998) Somatodendritic depolarization-activated potassium currents in rat neostriatal cholinergic interneurons are predominantly of the a type and attributable to coexpression of subunits. J Neurosci 18(9):3124–3137
Stiefel K, Gutkin B, Sejnowski T (2008) Cholinergic neuromodulation changes phase response curve shape and type in cortical pyramidal neurons. PLoS ONE 3(12):e3947
Surmeier D, Song W, Yan Z (1996) Coordinated expression of dopamine receptors in neostriatal medium spiny neurons. J Neurosci 16(20):6579–6591
Tan CO, Bullock D (2008) A dopamine-acetylcholine cascade: simulating learned and lesion-induced behavior of striatal cholinergic interneurons. J Neurophysiol 100(4):2409–2421
Terman D, Rubin JE, Yew A, Wilson C (2002) Activity patterns in a model for the subthalamopallidal network of the basal ganglia. J Neurosci 22(7):2963–2976
Wang Y, Rubin JE (2020) Complex bursting dynamics in an embryonic respiratory neuron model. Chaos 30(4):043127
Wilson C (2005) The mechanism of intrinsic amplification of hyperpolarizations and spontaneous bursting in striatal cholinergic interneurons. Neuron 45(4):575–585
Wilson C, Goldberg J (2006) Origin of the slow afterhyperpolarization and slow rhythmic bursting in striatal cholinergic interneurons. J Neurophysiol 95(1):196–204
Witten I, Lin S, Brodsky M, Prakash R, Diester I, Anikeeva P, Deisseroth K (2010) Cholinergic interneurons control local circuit activity and cocaine conditioning. Science 330(6011):1677–1681

Zhang W, Basile A, Gomeza J, Volpicelli L, Levey A, Wess J (2002) Characterization of central inhibitory muscarinic autoreceptors by the use of muscarinic acetylcholine receptor knock-out mice. J Neurosci 22(5):1709–1717

Zhang Y, Reynolds J, Cragg S (2018) Pauses in cholinergic interneuron activity are driven by excitatory input and delayed rectification, with dopamine modulation. Neuron 98(5):918–925

Zhou F, Wilson C, Dani J (2002) Cholinergic interneuron characteristics and nicotinic properties in the striatum. J Neurobiol 53(4):590–605

Zucca S, Zucca A, Nakano T, Aoki S, Wickens J (2018) Pauses in cholinergic interneuron firing exert an inhibitory control on striatal output in vivo. Elife 7:e32510